


# Control of electronic topology in a strongly correlated electron system

Received: 4 February 2022

Accepted: 12 September 2022

Published online: 29 September 2022

 Check for updates

Sami Dzsaber<sup>1</sup>, Diego A. Zocco<sup>1</sup>, Alix McCollam<sup>2</sup>, Franziska Weickert<sup>1,3</sup>, Ross McDonald<sup>3</sup>, Mathieu Taupin<sup>1</sup>, Gaku Eguchi<sup>1</sup>, Xinlin Yan<sup>1</sup>, Andrey Prokofiev<sup>1</sup>, Lucas M. K. Tang<sup>2</sup>, Bryan Vlaar<sup>2</sup>, Laurel E. Winter<sup>3</sup>, Marcelo Jaime<sup>3</sup>, Qimiao Si<sup>4</sup> & Silke Paschen<sup>1</sup>✉

It is becoming increasingly clear that breakthrough in quantum applications necessitates materials innovation. In high demand are conductors with robust topological states that can be manipulated at will. This is what we demonstrate in the present work. We discover that the pronounced topological response of a strongly correlated “Weyl-Kondo” semimetal can be genuinely manipulated—and ultimately fully suppressed—by magnetic fields. We understand this behavior as a Zeeman-driven motion of Weyl nodes in momentum space, up to the point where the nodes meet and annihilate in a topological quantum phase transition. The topologically trivial but correlated background remains unaffected across this transition, as is shown by our investigations up to much larger fields. Our work lays the ground for systematic explorations of electronic topology, and boosts the prospect for topological quantum devices.

Key to uncovering the richness of phenomena displayed by strongly correlated electron systems and to understanding the underlying mechanisms has been the great tunability of these systems, which enabled a systematic exploration of the landscape of their low-temperature phases<sup>1–4</sup>. As an example, such studies led to the discovery that high-temperature superconductivity is in many, if not all cases an emergent phase stabilized by quantum critical fluctuations<sup>5,6</sup>, and that critical electron delocalization transitions<sup>7,8</sup> may play an important role therein<sup>9</sup>. Such deep insight is indispensable to tailoring properties at will, and ultimately exploiting them for applications.

Electrons are strongly correlated if their mutual Coulomb repulsion reaches or exceeds the same order as their kinetic energy. In bulk materials, this regime is typically realized by means of *f* and/or *d* orbitals with a suitable strength of orbital overlap. Flat bands, renormalized by orders of magnitude compared to simple metals and pinned to the Fermi energy, can be achieved via the Kondo effect, driven by a spin exchange interaction between localized (typically 4*f*) and itinerant (*s*, *p*, *d*) electrons<sup>10</sup>. Recently, it has been demonstrated that such very strongly correlated conductors may also exhibit extreme signatures of nontrivial topology<sup>11</sup>. This raises the question as

to whether the excellent tunability in terms of correlation physics can also be exploited to control topology per se.

Our work shows that this can indeed be achieved. Upon tuning Ce<sub>3</sub>Bi<sub>4</sub>Pd<sub>3</sub><sup>12</sup>, a Weyl-Kondo semimetal<sup>11–13</sup>, by magnetic field we observe a continuous suppression of the giant topological response associated with the material's Kondo-driven Weyl nodes, and the annihilation of the nodes. This transition is characterized by the suppression of singularities in the Berry curvature instead of a Landau order parameter; as such, it is a topological quantum phase transition. An important and surprising aspect is that this transition happens in an only smoothly varying correlated background; one could instead have expected topological states to be essentially inert to tuning parameter changes. This discovery opens up a new regime in the correlation–topology interplay, and will facilitate a systematic search for new correlation-driven topological phases.

## Results and discussion

Before presenting our results and explaining them in detail, we summarize the key signatures of the Weyl-Kondo semimetal Ce<sub>3</sub>Bi<sub>4</sub>Pd<sub>3</sub> in zero magnetic field<sup>11,12</sup> (see Supplementary Note 1 for details). They are

<sup>1</sup>Institute of Solid State Physics, Vienna University of Technology, 1040 Vienna, Austria. <sup>2</sup>High Field Magnet Laboratory (HFML-EMFL), Radboud University, 6525 ED Nijmegen, The Netherlands. <sup>3</sup>Los Alamos National Laboratory, Los Alamos, NM 87545, USA. <sup>4</sup>Department of Physics and Astronomy, Rice Center for Quantum Materials, Rice University, Houston, TX 77005, USA. ✉e-mail: [paschen@ifp.tuwien.ac.at](mailto:paschen@ifp.tuwien.ac.at)

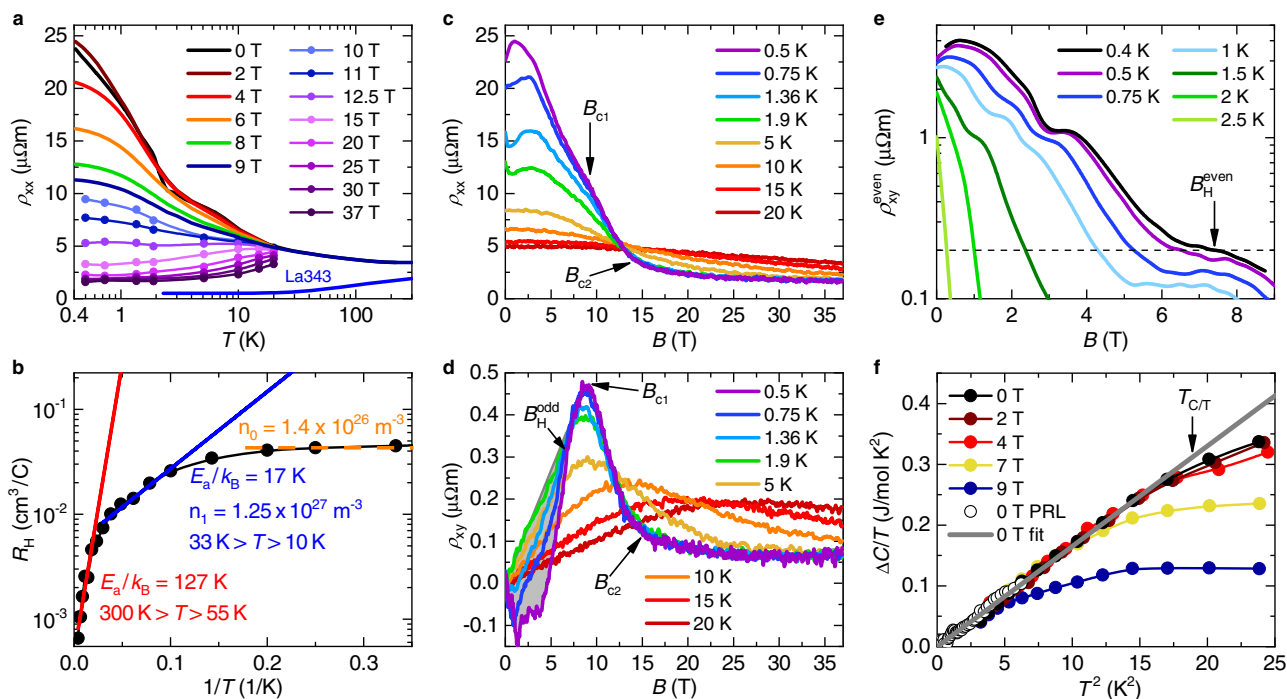
(i) an electronic specific heat coefficient  $\Delta C/T$  that is linear in  $T^2$ , with a giant slope, evidencing ultraslow quasiparticles with linear electronic dispersion<sup>12</sup>; and (ii) a giant spontaneous Hall effect as a result of Weyl nodes—sources and sinks of Berry curvature—pinned to the immediate vicinity of the Fermi level<sup>11</sup>. We note that the semimetallic ground state of  $\text{Ce}_3\text{Bi}_4\text{Pd}_3$  is well documented (Supplementary Note 2). As will be shown in what follows, the momentum-space separation of the Weyl nodes, which are positioned in a Kondo insulating background, is successively reduced with increasing magnetic field, until the Weyl nodes meet in momentum space and annihilate. Only at considerably larger magnetic fields, the Kondo insulator gap is quenched and the system becomes a heavy fermion metal (see Supplementary Note 3 and Supplementary Fig. 2 for a cartoon of the correlated electronic bandstructure). The latter transition has also been observed in<sup>14</sup>.

Figure 1 gives an overview of our electrical transport and specific heat data. Salient transport features in zero magnetic field are an electrical resistivity that increases moderately with decreasing temperature (Fig. 1a) and a linear-response Hall coefficient with two ranges of thermally activated behavior and a saturation to a constant value at the lowest temperatures (Fig. 1b). A plausible interpretation, which will receive further support from the field-dependent data presented below, is that this behavior results from a (pseudo)gapped background density of states, within which a narrow (Kondo insulator) gap forms at lower temperatures, against which a small residual density of states associated with the Fermi-level-bound Weyl nodes becomes apparent

at the lowest temperatures (see cartoon in Supplementary Fig. 2). The presence of a (pseudo)gap in the noninteracting density of states is in agreement with density functional theory (DFT) calculations, although the theoretical gap size is considerably larger<sup>15</sup>.

The application of magnetic fields gradually suppresses the low-temperature resistivity upturn. This is the case until, ultimately, metallic behavior is seen, albeit with higher resistivity and a different temperature dependence than in the nonmagnetic reference compound  $\text{La}_3\text{Bi}_4\text{Pd}_3$  (Fig. 1a). This indicates that Kondo physics is at play even at our largest field of 37 T. Isothermal magnetic-field-dependent measurements of the electrical resistivity  $\rho_{xx}(B)$  (Fig. 1c) and Hall resistivity  $\rho_{xy}(B)$  (Fig. 1d) reveal that this field-induced transformation occurs in two stages. The signatures thereof are most pronounced in the lowest-temperature data. Here, the electrical resistivity displays a shoulder at about 9 T and a crossover to almost field-independent behavior at about 14 T (see arrows labeled  $B_{c1}$  and  $B_{c2}$ , respectively, and Supplementary Note 4 for further analyses). The corresponding signatures in the Hall resistivity are kinks at the same two fields. A quantitative analysis, presented further below (Fig. 2), reveals that this behavior reflects a two-stage Fermi surface reconstruction at two quantum phase transitions.

We first examine the effect the magnetic field has on the material's topological characteristics. The most direct signature is a giant spontaneous as well as even-in-field nonlinear topological Hall effect, which evidences Berry curvature singularities from Weyl nodes in close



**Fig. 1 | Data overview and characteristic transport and thermodynamic scales of  $\text{Ce}_3\text{Bi}_4\text{Pd}_3$ .** **a** Temperature-dependent electrical resistivity at various fixed magnetic fields. For  $B > 9$  T, iso- $B$  cuts (dots) were taken from panel (c). The zero-field resistivity of the nonmagnetic reference compound  $\text{La}_3\text{Bi}_4\text{Pd}_3$  is shown for comparison. The small kink seen near 2.5 K in the zero-field data is associated with the onset of a giant spontaneous Hall voltage that, due to the large associated Hall angle, leaves an imprint also on the longitudinal resistivity<sup>11</sup>. The low-field data are taken from Ref. 11. **b** Arrhenius plot of the linear response normal (antisymmetrized) Hall coefficient  $R_H$  of  $\text{Ce}_3\text{Bi}_4\text{Pd}_3$  (black symbols). The black line is a guide to the eyes. Red and blue lines correspond to fits with  $R_H = R_{H,i} \exp[E_a/(k_B T)]$ , where  $n_i = 1/(R_{H,i} e)$  is the charge carrier concentration in a simple one-band model. Below 10 K, the data saturate to a constant value (dashed orange line), with the charge carrier concentration  $n_0$  (again in a one-band model). **c** Magnetoresistance isotherms in fields up to  $B = 37$  T, for various temperatures between 0.5 and 20 K.

**d** Normal (antisymmetrized) Hall resistivity isotherms at the same fields and temperatures.  $B_{c1}$  and  $B_{c2}$  are determined in Fig. 2. Below  $B_{c1}^{\text{odd}}$  (shown for the 0.5 K data), the anomalous Hall contribution (grey shading) leads to a deviation from the initial linear-in- $B$  normal Hall resistivity by more than 5%. **e** Even-in-field (symmetrized, see Supplementary Note 6) Hall resistivity isotherms at low temperatures and fields. Above  $B_{c1}^{\text{even}}$  (shown for the 0.4 K data) this Weyl-node derived signal drops to below 0.2, which is 5% of the maximum of the lowest-temperature isotherm (data from Ref. 11). **f** Temperature-dependent electronic specific heat coefficient (see Supplementary Note 5 for details) vs  $T^2$  at various fixed fields (open symbols are from Ref. 12). Above  $T_{C/T}$  (shown for the 0 T data), the data deviate by more than 5% from the low-temperature  $\Delta C/T = \Gamma T^2$  fit, which represents the linear Weyl dispersion. The spurious low-field features in the low-temperature resistivity isotherms (Fig. 1c) are imprints of the large Hall contributions, caused by the current path redistribution due to the large Hall angle<sup>11</sup>.

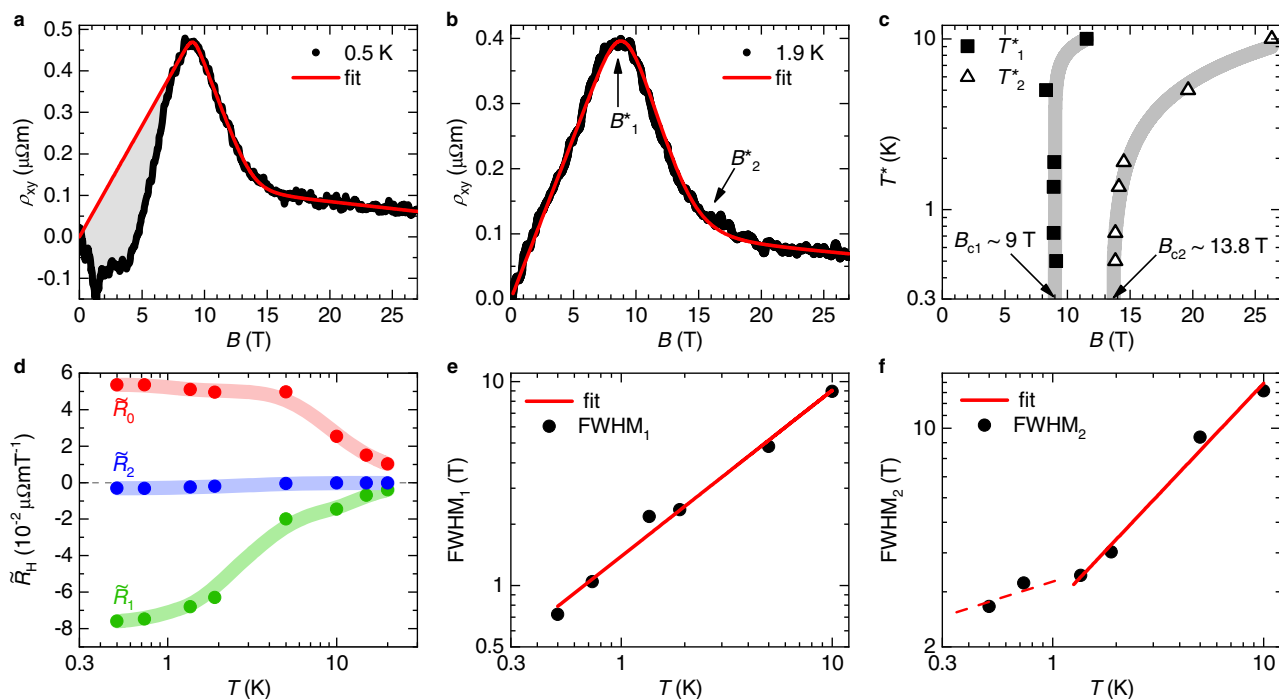


**Fig. 2 | Two-stage Fermi surface reconstruction in  $\text{Ce}_3\text{Bi}_4\text{Pd}_3$ .** **a** Hall resistivity vs applied magnetic field at 0.5 K, together with the best fit according to the two-crossovers model (see Supplementary Note 7). The deviation of the data from linear behavior (shaded grey area) is due to a Berry curvature-derived anomalous Hall contribution (Ref. 11). **b** Same as (a) at 1.9 K. The Berry-curvature derived contribution is essentially absent at this temperature. The two characteristic fields  $B_1^*$  and  $B_2^*$  mark the positions of the crossovers between the different regimes. **c** The crossover fields  $B_1^*(T)$  and  $B_2^*(T)$  determined from the  $\rho_{xy}(B)$  fits are plotted as  $T_1^*(B)$  and  $T_2^*(B)$ , respectively, in a temperature-magnetic field phase diagram. They extrapolate, in the zero-temperature limit, to  $B_{c1}$  and  $B_{c2}$  and separate three regimes

of simple (linear-in- $B$ ) normal Hall resistivity. **d** Differential Hall coefficients  $\tilde{R}_0$ ,  $\tilde{R}_1$ , and  $\tilde{R}_2$  of these three regimes, determined from the  $\rho_{xy}(B)$  fits, as function of temperature. The lines are guides to the eyes. **e** Width of the first crossover  $\text{FWHM}_1$ , representing the full width at half maximum of the second derivative of the two-crossovers fit function. The straight line is a pure power law fit,  $\text{FWHM}_1 \propto T^p$ , with  $p = 0.81$ . It describes the data down to the lowest temperature, evidencing that the carrier concentration changes abruptly at  $T = 0$ . **f** Same as in (e) for the second crossover. The straight full line is a pure power law fit,  $\text{FWHM}_2 \propto T^p$ , with  $p = 0.71$  to the data above 1 K. At lower temperatures, the rate of decrease is somewhat reduced (red dashed line).

vicinity to the Fermi energy<sup>11</sup>. Somewhat more indirect evidence is a temperature-dependent electronic specific heat that varies linearly in  $T^3$ , with a slope that even surpasses the (Debye-like) phonon contribution, and evidences linearly-dispersing electronic bands with ultralow velocity<sup>12,13</sup>. Together they have established the inversion symmetry (IS)-broken (noncentrosymmetric and nonsymmorphic) but time reversal symmetry (TRS)-preserving heavy fermion compound  $\text{Ce}_3\text{Bi}_4\text{Pd}_3$  as a model case of a strongly correlated topological semimetal<sup>11,12</sup> (see Supplementary Note 1 for further details).

In Fig. 1e we show how isothermal even-in-field (symmetrized and corrected for contact misalignment, see Supplementary Note 6 with Supplementary Fig. 5, and Ref. 11) topological Hall resistivities  $\rho_{xy}^{\text{even}}$  are successively suppressed by magnetic field. The apparent fine structure in this suppression, seen in the isotherms below 2 K, may reflect various regimes of Weyl node configurations in momentum space. Indeed, a rich sequence of Weyl node motion and annihilation under magnetic field tuning was found in Kondo model calculations on a diamond lattice<sup>16,17</sup>, which is an interesting topic for further investigations. Here, we focus on the ultimate total suppression of the effect, which occurs at  $B_{\text{H}}^{\text{even}}$  (see arrow in Fig. 1e for the lowest temperature isotherm). Also the linear-in- $T^3$  electronic specific heat (corresponding to an electronic specific heat coefficient  $\Delta C/T = \Gamma T^2$ , see Supplementary Note 5 for details) is successively suppressed by magnetic fields, which we quantify by the parameter  $T_{C/\Gamma}$  (see arrow in Fig. 1f on the zero-field curve). Interestingly, this suppression happens at constant  $\Gamma$ , indicating that the shape (slope and energy) of the Weyl dispersion remains unchanged as the Weyl nodes move in momentum space. Finally, we point to another feature that accompanies these two key signatures. It appears as an anomaly in the (normal, antisymmetrized and thus

odd-in-field) Hall resistivity isotherms (see arrow denoting  $B_{\text{H}}^{\text{odd}}$  as upper end of the grey shading, marked on the lowest-temperature isotherm in Fig. 1d) and is known as the anomalous topological Hall effect in TRS-broken Weyl semimetals<sup>18</sup>. It is associated with a magnetic field-induced even-in-momentum Berry curvature, which is in addition to the intrinsic (zero-field) odd-in-momentum Berry curvature of  $\text{Ce}_3\text{Bi}_4\text{Pd}_3$  (see also Ref. 11).

All these results together establish that magnetic field quenches the topological response, apparently via a process that moves the Weyl nodes at equal energy in momentum space. This raises the following questions: Which mechanism underlies this effect? Does magnetic field suppress the Kondo effect just as increasing the temperature above the Kondo coherence scale does<sup>11</sup>, thereby removing the correlated electrons and thus the basis for the Weyl-Kondo semimetal formation? Or did we succeed to annihilate the Weyl nodes in an intact Kondo coherent system? The Kondo-like electrical resistivity in 37 T suggests that some form of Kondo correlations persist. To show that the magnetic field indeed controls Kondo-driven Weyl nodal excitations, however, what needs to be established is that the Kondo effect as realized in zero magnetic field operates over the entire field range with topological response. We now turn to the search for such evidence.

We start with a quantitative analysis of the (normal, anti-symmetrized) Hall resistivity isotherms  $\rho_{xy}(B)$  of Fig. 1d. As established previously<sup>7</sup>, when magnetic field drives transitions between ground states with different Fermi volumes, the resulting (finite temperature) crossovers manifest as (broadened) kinks in  $\rho_{xy}(B)$ , and (broadened) steps in the differential Hall coefficient  $\tilde{R}_{\text{H}}(B) = \partial \rho_{xy}(B) / \partial B$ . Such behavior has been observed in a number of heavy fermion metals<sup>7,19–21</sup> driven by magnetic field across quantum critical points. From fits with

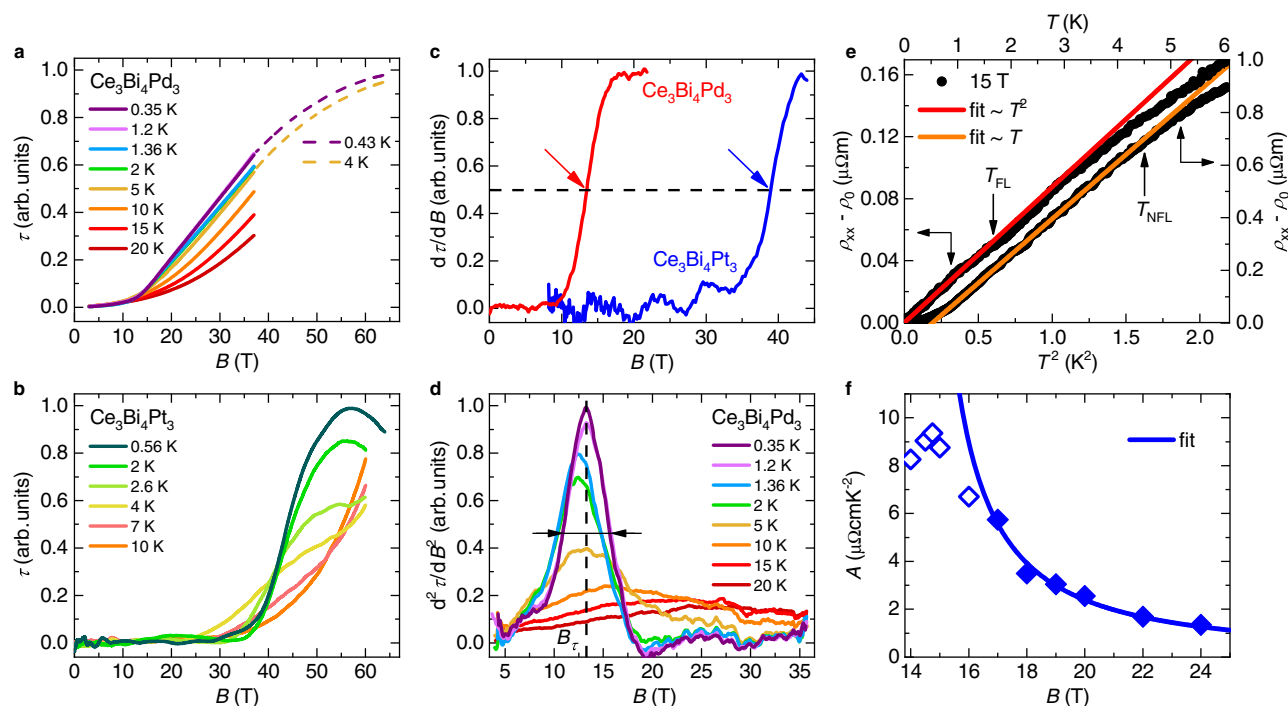


**Fig. 3 | Field-tuned Kondo insulator to heavy fermion metal transition in  $\text{Ce}_3\text{Bi}_4\text{Pd}_3$ .** **a** Magnetic torque isotherms of  $\text{Ce}_3\text{Bi}_4\text{Pd}_3$  at various temperatures as function of applied magnetic field up to 37 T and, for low temperatures, up to 65 T. **b** Same as in (a) for the Kondo insulator  $\text{Ce}_3\text{Bi}_4\text{Pt}_3$ . **c** Field derivative of the magnetic torque isotherms of  $\text{Ce}_3\text{Bi}_4\text{Pd}_3$  and  $\text{Ce}_3\text{Bi}_4\text{Pt}_3$  at the lowest temperatures, revealing similar characteristics, albeit at different fields (the fields where the step-like increases reach half height are indicated by arrows). **d** Second field derivative of the torque signal of  $\text{Ce}_3\text{Bi}_4\text{Pd}_3$ . We define the characteristic field  $B_c$  of the torque signal as the center of the width at half maximum, as indicated by the dashed vertical line

and the horizontal arrows for the 0.35 K isotherm. **e** Electrical resistivity of  $\text{Ce}_3\text{Bi}_4\text{Pd}_3$  at 15 T, displaying linear-in- $T^2$  Fermi liquid behavior from the lowest temperature of 0.1 K up to  $T_{\text{FL}}$  (bottom and left axes, red line; above  $T_{\text{FL}}$ , the data deviate by more than 5% from the Fermi liquid form  $\rho = \rho_0 + AT^2$ ) and linear-in- $T$  non-Fermi liquid behavior from somewhat above  $T_{\text{FL}}$  up to  $T_{\text{NFL}}$  (top and right axes, orange line; see Supplementary Note 11 for details). **f** Fermi liquid  $A$  coefficient vs applied magnetic field. The data above 16 T are well described by  $A \propto (B - B_{c2})^{-p}$  with  $B_{c2} = 13.8$  T and  $p \approx 1$ . Deviations at lower fields are attributed to proximity to the Kondo insulating phase (see Supplementary Note 11 and Supplementary Fig. 11).

a phenomenological crossover function<sup>7</sup> (see Supplementary Note 7 for details) one can extract not only the  $\bar{R}_H$  values associated with the different phases, but also the crossover fields  $B'$  and sharpnesses, quantified by the full width at half maximum (FWHM). In Fig. 2a, b we show two representative fits, for data at 0.5 K (for which we have subtracted the above-discussed anomalous topological Hall effect contribution) and 1.9 K, respectively. Fits of similar quality are obtained at all temperatures up to 10 K (Supplementary Fig. 6). At higher temperatures, we lose track of the two-stage nature and thus this model does no longer give meaningful results. Note that anomalous (nontopological) Hall contributions and multiband effects do not play significant roles here (see Supplementary Notes 8 and 9). The temperature-dependent fit parameters are shown in Fig. 2c–f. The two crossover fields  $B'_1$  and  $B'_2$  (Fig. 2b), determined for all available isotherms, are plotted as characteristic temperatures  $T'_1(B)$  and  $T'_2(B)$  in Fig. 2c. The extrapolations to  $T = 0$  of these curves identify  $B_{c1}$  and  $B_{c2}$  (see arrows in Fig. 2c). Both crossovers sharpen considerably with decreasing temperature (Fig. 2e, f), indicating that the phase diagram of magnetic field-tuned  $\text{Ce}_3\text{Bi}_4\text{Pd}_3$  comprises three phases with distinct Fermi volumes: a phase below  $B_{c1}$  with a small hole-like Fermi volume, an intermediate-field phase between  $B_{c1}$  and  $B_{c2}$  with an even smaller electron-like Fermi volume, and a high-field phase beyond  $B_{c2}$  with a much larger Fermi volume.

To understand this behavior and elucidate the character of these phases we have carried out torque magnetometry measurements. At low magnetic fields, and in particular across  $B'_1(T)$ , no sizable torque signal is detected (Fig. 3a), thus ruling out that a magnetic phase transition occurs at this field (see Supplementary Note 10 and Supplementary Fig. 10). A pronounced torque signal appears only above about 14 T; it corresponds to the onset of nonlinearity in the

magnetization<sup>14</sup>. Similar behavior, albeit with a much larger magnetic field scale, is also seen in the canonical Kondo insulator  $\text{Ce}_3\text{Bi}_4\text{Pt}_3$ , which we have studied for comparison (Fig. 3b). The corresponding characteristics in the first and second derivative with respect to the magnetic field are a step-like increase and a maximum, respectively. For  $\text{Ce}_3\text{Bi}_4\text{Pt}_3$ , the step in the lowest temperature isotherm occurs at 38.9 T (blue arrow in Fig. 3c), which is close to the field where a Kondo insulator to metal transition has previously been evidenced by a jump of the Sommerfeld coefficient<sup>22</sup>. The very similar feature seen for  $\text{Ce}_3\text{Bi}_4\text{Pd}_3$  (red curve in Fig. 3c) then suggests that also in this system a Kondo insulator to metal transition takes place, albeit at much lower fields. As characteristic field  $B_c$  of this transition, which is well-defined for all isotherms, we use the middle field at half height of the second derivative curves (Fig. 3d).

We also performed temperature-dependent electrical resistivity measurements at fields around this Kondo insulator to metal transition. On the high-field side of the transition, we observe Fermi liquid behavior,  $\rho = \rho_0 + AT^2$  (see Fig. 3e, bottom and left axes, for data at 15 T). This confirms that  $\text{Ce}_3\text{Bi}_4\text{Pd}_3$  has indeed metallized. The  $A$  coefficient measures the strength of electronic correlations. Values in the range of several  $\mu\Omega\text{cm}/\text{K}^2$ , as observed here, are typical of heavy fermion metals<sup>23</sup> (see Supplementary Note 11 for details). Thus, the quenching of the Kondo insulator gap by the magnetic field has indeed (as already indicated by the high-field resistivity curves in Fig. 1a) still not suppressed the Kondo interaction. Thus, what happens at  $B_{c2}$  is a field-induced Kondo insulator to heavy fermion metal transition, which was also studied in Ref. 14. In Fig. 3f we plot the  $A$  coefficient determined also for other fields (see Supplementary Fig. 11) as function of the magnetic field. Upon approaching the transition from the high-field side, the  $A$  coefficient increases, and is well described by a



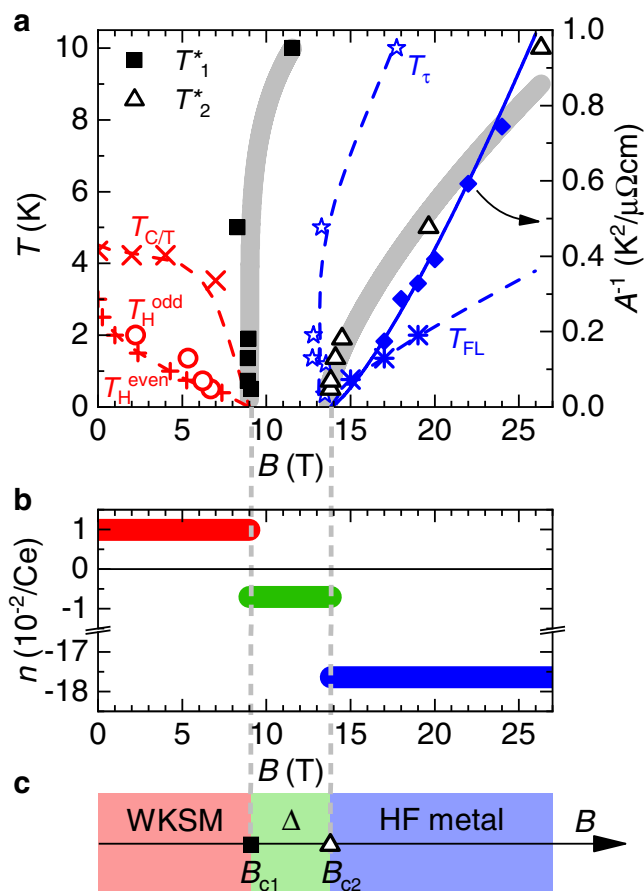


**Fig. 4 | Magnetic-field tuned phase diagram of  $\text{Ce}_3\text{Bi}_4\text{Pd}_3$ .** **a** Temperature-magnetic field phase diagram with the crossover temperatures  $T_1^*$  and  $T_2^*$  (from Fig. 2c), the temperature scales  $T_{C/T}$ ,  $T_H^{\text{even}}$ , and  $T_H^{\text{odd}}$  (all from Fig. 1) associated with the Weyl-Kondo semimetal phase, the characteristic scales  $T_\tau$  of the torque signal and  $T_{\text{FL}}$  of Fermi liquid behavior (both from Fig. 3) (all left axis). The inverse  $A$  coefficient (from Fig. 3) is plotted on the right axis, indicating an effective mass divergence at  $B_{c2}$ . **b** Effective charge carrier concentration in a single-band model,  $n = 1/(Re)$ , at the lowest temperature of 0.5 K (from Fig. 2d), in the three different magnetic field ranges. **c** Axis across a theoretical zero-temperature phase diagram. A topological quantum phase transition between a Weyl-Kondo semimetal (WKS) and a phase with annihilated and thus gapped-out Weyl nodes ( $\Delta$ ) occurs at  $B_{c1}$ . The underlying Kondo insulator gap persists across both the WKS and the  $\Delta$  phase, and is quenched only at a quantum critical point at  $B_{c2}$  to reach a heavy fermion (HF) metal phase at high fields.

divergence,  $A \propto 1/(B - B_{c2})$ , with the critical field  $B_{c2} = 13.8$  T from the Hall resistivity analysis (see caption of Fig. 3 for details). Such behavior is known from heavy fermion metals tuned by a magnetic field to a quantum critical point (QCP)<sup>21,24</sup>. In this case, also non-Fermi liquid (NFL) behavior should develop<sup>25,26</sup>, which we indeed observe in the form of a linear-in-temperature resistivity at 15 T, at temperatures above the Fermi liquid behavior seen at the lowest temperatures (Fig. 3e, top and right axes). This confirms that, at 15 T,  $\text{Ce}_3\text{Bi}_4\text{Pd}_3$  is slightly away from a QCP. Closer to the expected quantum critical field  $B_{c2}$ , the resistivity appears to be influenced by the nearby Kondo insulator phase, as seen by a rapid suppression of the  $A$  coefficient and a crossover to  $T^2$  behavior with a negative slope (Supplementary Fig. 11h), as well as an increase of the residual resistivity  $\rho_0$  not only towards but even across  $B_{c2}$  (Supplementary Fig. 11i). Whether these (nonmetallic) characteristics are generic to field-induced Kondo insulator to heavy fermion metal transitions is an interesting topic for future studies (we note that in a related pressure-induced transition in  $\text{SmB}_6$  no such effects were seen<sup>27,28</sup>, but this may reflect the need of

extending those measurements down to the temperature range of dilution refrigerators). Clearly, they do not represent normal (metallic) behavior and thus we define the upper boundary of Fermi liquid behavior  $T_{\text{FL}}$  (see arrows in Fig. 3e and Supplementary Fig. 11) only in the field range where these effects have minor influence. We conclude that a heavy Fermi liquid phase exists at fields above  $B_{c2}$ . In turn, this implies that the Kondo effect as operating at  $B = 0$  remains intact across  $B_{c1}$ .

We are now in the position to construct a temperature-magnetic field phase diagram that assembles the above-discussed characteristics (Fig. 4a). At low fields, these are  $T_{C/T}(B)$ ,  $T_H^{\text{even}}(B)$ , and  $T_H^{\text{odd}}(B)$ , all denoting temperatures up to which, at a given field, a certain signature of Weyl-Kondo semimetal behavior is detected. These scales all collapse at a critical field  $B_{c1}$  of 9 T. Importantly, the correlated background remains essentially unchanged across this field and no magnetic phase transition takes place. At high fields, we plot the scales  $T_\tau(B)$  and  $T_{\text{FL}}(B)$  associated with the torque anomaly and Fermi liquid behavior, respectively, and also include the inverse of the Fermi liquid resistivity coefficient,  $1/A$ , which hits zero at the effective mass divergence. In addition, we show the  $T_1^*(B)$  and  $T_2^*(B)$  scales extracted from our quantitative Hall resistivity analysis. Note that all these temperature scales are crossovers; they do not represent phase boundaries in the thermodynamic sense as none of the phases is associated with an order parameter.

In Fig. 4b we plot the charge carrier concentration  $n$  (in units of carriers per Ce atom) of the three phases, extracted in a single-band model from the lowest-temperature values of the differential Hall coefficients (Fig. 2d). It changes from about 0.01 holes below  $B_{c1}$ , via 0.007 electrons between  $B_{c1}$  and  $B_{c2}$ , to 0.18 electrons beyond  $B_{c2}$ . The 25-fold increase across  $B_{c2}$  is independent evidence for the above-discussed Kondo insulator to heavy fermion metal transition. The more modest reduction of the absolute value of the carrier concentration across  $B_{c1}$  indicates a Fermi surface reconstruction that involves only a fraction of momentum space. The annihilation and associated gapping-out of Weyl nodes is exactly such a phenomenon. Also the sign change of  $n$  across  $B_{c1}$  can be understood in this scenario (see Supplementary Note 12 and Supplementary Fig. 12). That  $n$  is field independent below  $B_{c1}$  (as seen from the linear-in-field behavior of the Hall resistivity in this regime, Fig. 2b) confirms that magnetic field moves the Weyl nodes at constant energy. The only process that can then remove them is their mutual annihilation, which we thus propose to happen at  $B_{c1}$ . Importantly, this takes place in a background of unchanged symmetry and with the Kondo effect continuing to operate. In other words, we have realized a controlled suppression of the Kondo-driven topological semimetal. A corollary is that we have isolated the tuning of topology from the tuning of correlation physics as such.

In Fig. 4c we summarize these findings in a schematic zero-temperature phase diagram. The low-field phase is a Weyl-Kondo semimetal (WKS)<sup>11–13</sup> that, as evidenced here, consists of Weyl nodes situated within the narrow energy gap of a Kondo insulator. As function of magnetic field a sequence of two Fermi volume-changing quantum phase transitions is observed. At  $B_{c1}$ , all signatures of the Weyl-Kondo semimetal disappear as the Weyl nodes annihilate in a topological quantum phase transition. At  $B_{c2}$ , the Kondo insulator with gapped-out Weyl nodes (denoted by the symbol  $\Delta$ ) transforms into a heavy fermion (HF) metal, in a transition that displays signatures of quantum criticality and must thus be at least nearly continuous.

This raises the question of why the phenomena of genuine topology tuning and Weyl node annihilation have remained elusive in the much more extensively studied noninteracting regime<sup>29</sup>? A magnetic field can either act on the spin (via the Zeeman effect) or the charge of an electron (via the orbital effect). In Kondo systems the former dominates, in high-mobility semimetals the latter. The momentum space motion of Weyl nodes requires sizable Zeeman coupling<sup>16,17</sup>. In its absence<sup>30</sup>, field-driven changes of topological

signatures<sup>31,32</sup> can arise from orbital effects such as the tunneling between zeroth Landau level states of adjacent Weyl nodes<sup>31</sup>, at finite Weyl node separation. Of course, also changes in a material's broken symmetry state can be accompanied by changes of topology<sup>33</sup>, but this is not the topic of interest to us here (see Supplementary Notes 13 and 14 for further details).

In summary, we have demonstrated the genuine control of Weyl nodes, with clarity and ease. The clarity is attributed to the fact that in Ce<sub>3</sub>Bi<sub>4</sub>Pd<sub>3</sub> the Weyl nodes form within a (strongly correlated, Kondo insulating) gapped state and are positioned in close vicinity of the Fermi energy. Because topologically trivial states are gapped out, there is no need to disentangle Weyl fermions from topologically trivial carriers, which hampers the field of weakly interacting Weyl semimetals. The ease of control—namely that a rather modest field of 9 T was not only enough to manipulate the positions of the Weyl nodes in momentum space, but even drive their annihilation—shows that the well-known excellent tunability of (topologically trivial) strongly correlated electron systems<sup>1–4</sup> holds also for topological features in such systems. As such, our study lays the ground for establishing a global phase diagram for strongly correlated topological materials. Key open questions to address include whether the phases and transitions discovered here exist also in other materials and are thus universal, and whether quantum criticality plays an important role in stabilizing them. The latter is hinted at by recent inelastic neutron scattering experiments<sup>34</sup>.

Our findings may also guide investigations in related materials classes. Much effort is currently devoted to artificial materials such as twisted bilayer systems where correlations can be enhanced via a moiré potential<sup>35–38</sup>. Additional tuning knobs in such heterostructures are the dielectric displacement and electrostatic doping, which may become powerful if further advances towards highly reproducible structures can be accomplished. Finally, we point to the potential of strongly correlated bulk materials such as Ce<sub>3</sub>Bi<sub>4</sub>Pd<sub>3</sub> for quantum devices<sup>4,39–41</sup>, where the robust and giant topological response—together with the high level of topology control demonstrated here—opens new opportunities. As an example we name microwave nonreciprocity at zero magnetic field, a key functionality needed in circuit quantum electrodynamics systems<sup>42</sup>, that could be realized via the spontaneous Hall response of Ce<sub>3</sub>Bi<sub>4</sub>Pd<sub>3</sub>.

## Methods

### Synthesis

Single crystals of Ce<sub>3</sub>Bi<sub>4</sub>Pd<sub>3</sub>, Ce<sub>3</sub>Bi<sub>4</sub>Pt<sub>3</sub>, and of the nonmagnetic reference compound La<sub>3</sub>Bi<sub>4</sub>Pd<sub>3</sub> were grown using the flux method. For Ce<sub>3</sub>Bi<sub>4</sub>Pt<sub>3</sub>, elementary Ce, Pt, and Bi in an atomic ratio of 1:1:7 were placed in an alumina crucible, and heated to 1100°C in a vacuum-sealed quartz tube, using a box furnace. The melt was then slowly cooled to 600°C after a dwell time of 12 h at 1100°C, with a cooling rate of 1°C/h, and then left annealing for 12 h. Crystals of typically 1 mm in diameter were then extracted from the melt using a centrifuge. For Ce<sub>3</sub>Bi<sub>4</sub>Pd<sub>3</sub> and La<sub>3</sub>Bi<sub>4</sub>Pd<sub>3</sub>, as the primary stable phases at Bi excess are CeBi<sub>2</sub>Pd and LaBi<sub>2</sub>Pd, the Bi content was strongly reduced to about 1:1.5 (see also Ref. 12). The chemical composition and crystal structure of the samples were determined by energy dispersive x-ray spectroscopy and powder x-ray diffraction. Laue diffraction was utilized to determine the crystallographic orientation of selected samples.

### Measurement setups

**High-field experiments.** Magnetoresistance, Hall effect, and torque magnetization measurements in DC fields up to 37 T were performed at the HFML-EMFL facility at Nijmegen. Magnetotransport data were measured using Stanford Research SR830 lock-in amplifiers, with the measured voltage signal pre-amplified 100 times using Princeton Applied Research low-noise transformers. Electrical contacts were made by either spot welding or gluing with silver paint 12 µm diameter gold wires to the samples in a 5-wire configuration. All displayed Hall

resistivity curves were obtained by the standard antisymmetrizing procedure of the resistivity  $\rho_{xy}^{\text{meas}}$  measured across the Hall contacts, i.e.,  $\rho_{xy}(B) = [\rho_{xy}^{\text{meas}}(+B) - \rho_{xy}^{\text{meas}}(-B)]/2$ . This cancels out both the spontaneous Hall effect (zero-field signal) and any even-in-field component. Torque and magnetization measurements in pulsed fields up to 65 T were performed at the NHMFL-LANL facility at Los Alamos. Magnetization data were obtained only for Ce<sub>3</sub>Bi<sub>4</sub>Pt<sub>3</sub>, using an extraction magnetometer and the "sample-in/sample-out" technique to separate the sample signal from the background. In this case, the magnetic field was not aligned to any particular crystallographic axis. In all torque experiments, piezo-cantilevers were used for enhanced sensitivity. Samples were attached to the levers with Dow Corning high vacuum grease. The measured torque signal was obtained after balancing a Wheatstone bridge containing the resistance of the sample's cantilever and a "dummy" (empty lever) resistor. Due to the small samples required for this technique, the magnetic field was initially not aligned to any particular crystallographic axis. A sample rotator was used to scan the torque signal across different orientations. In all cases, temperatures down to 0.35 K were obtained using a <sup>3</sup>He cryostat.

**Low-temperature experiments.** Additional magnetoresistance, Hall effect, and specific heat measurements were obtained in Vienna using a Quantum Design Physical Property Measurement System, equipped with <sup>3</sup>He options. Low-temperature electrical resistivity measurements down to 70 mK and in magnetic fields up to 15 T were performed in an Oxford dilution refrigerator.

## Data availability

All data that are necessary to interpret, verify, and extend the presented research are contained in the main part of this article. They are provided through deposition in the repository Zenodo (<https://doi.org/10.5281/zenodo.7043820>).

## References

1. Tokura, Y. & Nagaosa, N. Orbital physics in transition-metal oxides. *Science* **288**, 462 (2000).
2. v. Löhneysen, H., Rosch, A., Vojta, M. & Wölfle, P. Fermi-liquid instabilities at magnetic quantum critical points. *Rev. Mod. Phys.* **79**, 1015 (2007).
3. Keimer, B., Kivelson, S. A., Norman, M. R., Uchida, S. & Zaanen, J. From quantum matter to high-temperature superconductivity in copper oxides. *Nature* **518**, 179 (2015).
4. Paschen, S. & Si, Q. Quantum phases driven by strong correlations. *Nat. Rev. Phys.* **3**, 9–26 (2021).
5. Mathur, N. et al. Magnetically mediated superconductivity in heavy fermion compounds. *Nature* **394**, 39–43 (1998).
6. Michon, B. et al. Thermodynamic signatures of quantum criticality in cuprate superconductors. *Nature* **567**, 218 (2019).
7. Paschen, S. et al. Hall-effect evolution across a heavy-fermion quantum critical point. *Nature* **432**, 881 (2004).
8. Prochaska, L. et al. Singular charge fluctuations at a magnetic quantum critical point. *Science* **367**, 285 (2020).
9. Badoux, S. et al. Change of carrier density at the pseudogap critical point of a cuprate superconductor. *Nature* **531**, 210–214 (2016).
10. Hewson, A. C. *The Kondo Problem to Heavy Fermions* (Cambridge University Press, Cambridge, 1997).
11. Dzsaber, S. et al. Giant spontaneous Hall effect in a nonmagnetic Weyl-Kondo semimetal. *Proc. Natl. Acad. Sci. U.S.A.* **118**, e2013386118 (2021).
12. Dzsaber, S. et al. Kondo insulator to semimetal transformation tuned by spin-orbit coupling. *Phys. Rev. Lett.* **118**, 246601 (2017).
13. Lai, H.-H., Greife, S. E., Paschen, S. & Si, Q. Weyl-Kondo semimetal in heavy-fermion systems. *Proc. Natl. Acad. Sci. USA.* **115**, 93 (2018).
14. Kushwaha, S. K. et al. Magnetic field-tuned Fermi liquid in a Kondo insulator. *Nat. Commun.* **10**, 5487 (2019).

15. Tomczak, J. M. Thermoelectricity in correlated narrow-gap semi-conductors. *J. Phys.: Condens. Matter* **30**, 183001 (2018).
16. Greife, S. E., Lai, H.-H., Paschen, S. & Si, Q. Weyl-Kondo semimetal: towards control of Weyl nodes. *JPS Conf. Proc.* **30**, 011013 (2020).
17. Greife, S. E., Lai, H.-H., Paschen, S. & Si, Q. Extreme response of Weyl-Kondo semimetal to Zeeman coupling. *arXiv:2012.15841* (2020).
18. Nagaosa, N., Sinova, J., Onoda, S., MacDonald, A. H. & Ong, N. P. Anomalous Hall effect. *Rev. Mod. Phys.* **82**, 1539 (2010).
19. Friedemann, S. et al. Fermi-surface collapse and dynamical scaling near a quantum-critical point. *Proc. Natl. Acad. Sci. USA* **107**, 14547 (2010).
20. Custers, J. et al. Destruction of the Kondo effect in the cubic heavy-fermion compound  $\text{Ce}_3\text{Pd}_{20}\text{Si}_6$ . *Nat. Mater.* **11**, 189 (2012).
21. Martelli, V. et al. Sequential localization of a complex electron fluid. *Proc. Natl. Acad. Sci. U.S.A.* **116**, 17701 (2019).
22. Jaime, M. et al. Closing the spin gap in the Kondo insulator  $\text{Ce}_3\text{Bi}_4\text{Pt}_3$  at high magnetic fields. *Nature* **405**, 160 (2000).
23. Kadowaki, K. & Woods, S. B. Universal relationship of the resistivity and specific heat in heavy-fermion compounds. *Solid State Commun.* **58**, 507–509 (1986).
24. Gegenwart, P. et al. Magnetic-field induced quantum critical point in  $\text{YbRh}_2\text{Si}_2$ . *Phys. Rev. Lett.* **89**, 056402 (2002).
25. Si, Q., Rabello, S., Ingersent, K. & Smith, J. Locally critical quantum phase transitions in strongly correlated metals. *Nature* **413**, 804 (2001).
26. Custers, J. et al. The break-up of heavy electrons at a quantum critical point. *Nature* **424**, 524 (2003).
27. Gabáni, S. et al. Pressure-induced Fermi-liquid behavior in the Kondo insulator  $\text{SmB}_6$ : Possible transition through a quantum critical point. *Phys. Rev. B* **67**, 172406 (2003).
28. Zhou, Y. et al. Quantum phase transition and destruction of Kondo effect in pressurized  $\text{SmB}_6$ . *Sci. Bull.* **62**, 1439 (2017).
29. Armitage, N. P., Mele, E. J. & Vishwanath, A. Weyl and Dirac semimetals in three-dimensional solids. *Rev. Mod. Phys.* **90**, 015001 (2018).
30. Baidya, S. & Vanderbilt, D. First-principles theory of the Dirac semimetal  $\text{Cd}_3\text{As}_2$  under Zeeman magnetic field. *Phys. Rev. B* **102**, 165115 (2020).
31. Ramshaw, B. J. et al. Quantum limit transport and destruction of the Weyl nodes in TaAs. *Nat. Commun.* **9**, 2217 (2018).
32. Liang, T. et al. A pressure-induced topological phase with large Berry curvature in  $\text{Pb}_{1-x}\text{Sn}_x\text{Te}$ . *Sci. Adv.* **3** (2017).
33. Schoop, L. M. et al. Tunable Weyl and Dirac states in the non-symorphic compound  $\text{CeSbTe}$ . *Sci. Adv.* **4**, eaar2317 (2018).
34. Fuhrman, W. T. et al. Pristine quantum criticality in a Kondo semimetal. *Sci. Adv.* **7** (2021).
35. Bistrizter, R. & MacDonald, A. H. Moiré bands in twisted double-layer graphene. *Proc. Natl. Acad. Sci. U.S.A.* **108**, 12233 (2011).
36. Cao, Y. et al. Unconventional superconductivity in magic-angle graphene superlattices. *Nature* **556**, 43–50 (2018).
37. Choi, Y. et al. Correlation-driven topological phases in magic-angle twisted bilayer graphene. *Nature* **589**, 536–541 (2021).
38. Kennes, D. M. et al. Moiré heterostructures as a condensed-matter quantum simulator. *Nat. Phys.* **17**, 155–163 (2021).
39. de Leon, N. P. et al. Materials challenges and opportunities for quantum computing hardware. *Science* **372**, eabb2823 (2021).
40. Ball, P. Quantum materials: where many paths meet. *MRS Bulletin* **42**, 698 (2017).
41. Keimer, B. & Moore, J. E. The physics of quantum materials. *Nat. Phys.* **13**, 1045 (2017).
42. Viola, G. & DiVincenzo, D. P. Hall effect gyrators and circulators. *Phys. Rev. X* **4**, 021019 (2014).

## Acknowledgements

The authors wish to thank H.-H. Lai, S. E. Greife, and A. P. Higginbotham for fruitful discussions. We acknowledge support of the HFML-RU/NWO-I, member of the European Magnetic Field Laboratory (EMFL). A portion of this work was performed at the National High Magnetic Field Laboratory, which is supported by the National Science Foundation Cooperative Agreement No. DMR-1157490 and DMR-1644779, the State of Florida and the United States Department of Energy. M.J. acknowledges support from the US DOE Basic Energy Science project “Science at 100T”. The work in Vienna was supported by the Austrian Science Fund (I2535, S.P.; I4047, D.Z.; 29279, S.P.; I5868–FOR5249, S.P.), the European Union’s Horizon 2020 Research and Innovation Programme (824109-EMP, S.P.), and the European Research Council (ERC Advanced Grant 101055088-CorMeTop, S.P.). The work at Rice was in part supported by the NSF (DMR-2220603, Q.S.), the AFOSR (FA9550-21-1-0356, Q.S.), and the Robert A. Welch Foundation (C-1411, Q.S.).

## Author contributions

S.P. designed and guided the research. X.Y. and A.P. synthesized and characterized the material. S.D., D.Z., A.M., F.W., R.M., L.T., B.V., L.E.W., and M.J. performed the high-field experiments, M.T., S.D., G.E., and D.Z. the low-temperature experiments. S.D. analyzed the data, with contributions from D.Z., M.T., G.E., and S.P. The manuscript was written by S.P., with contributions from S.D., D.Z., and Q.S. All authors contributed to the discussion.

## Competing interests

The authors declare no competing interests.

## Additional information

**Supplementary information** The online version contains supplementary material available at <https://doi.org/10.1038/s41467-022-33369-8>.

**Correspondence** and requests for materials should be addressed to Silke Paschen.

**Peer review information** *Nature Communications* thanks Shuang Jia and the other, anonymous, reviewer(s) for their contribution to the peer review of this work. Peer reviewer reports are available.

**Reprints and permission information** is available at <http://www.nature.com/reprints>

**Publisher’s note** Springer Nature remains neutral with regard to jurisdictional claims in published maps and institutional affiliations.

**Open Access** This article is licensed under a Creative Commons Attribution 4.0 International License, which permits use, sharing, adaptation, distribution and reproduction in any medium or format, as long as you give appropriate credit to the original author(s) and the source, provide a link to the Creative Commons license, and indicate if changes were made. The images or other third party material in this article are included in the article’s Creative Commons license, unless indicated otherwise in a credit line to the material. If material is not included in the article’s Creative Commons license and your intended use is not permitted by statutory regulation or exceeds the permitted use, you will need to obtain permission directly from the copyright holder. To view a copy of this license, visit <http://creativecommons.org/licenses/by/4.0/>.

© The Author(s) 2022, corrected publication 2022

# Supplementary Information

## Control of electronic topology in a strongly correlated electron system

Sami Dzsaber<sup>1</sup>, Diego A. Zocco<sup>1</sup>, Alix McCollam<sup>2</sup>, Franziska Weickert<sup>3</sup>, Ross McDonald<sup>3</sup>, Mathieu Taupin<sup>1</sup>, Gaku Eguchi<sup>1</sup>, Xinlin Yan<sup>1</sup>, Andrey Prokofiev<sup>1</sup>, Lucas M. K. Tang<sup>2</sup>, Bryan Vlaar<sup>2</sup>, Laurel E. Winter<sup>3</sup>, Marcelo Jaime<sup>3</sup>, Qimiao Si<sup>4</sup>, and Silke Paschen<sup>1,\*</sup>

<sup>1</sup>*Institute of Solid State Physics, Vienna University of Technology, 1040 Vienna, Austria*

<sup>2</sup>*High Field Magnet Laboratory (HFML-EMFL), Radboud University,  
6525 ED Nijmegen, The Netherlands*

<sup>3</sup>*Los Alamos National Laboratory, Los Alamos, NM 87545, USA*

<sup>4</sup>*Department of Physics and Astronomy, Rice Center for Quantum Materials, Rice University, Houston, TX  
77005, USA*

### Supplementary Note 1: Summary of Weyl-Kondo characteristics of $\text{Ce}_3\text{Bi}_4\text{Pd}_3$

$\text{Ce}_3\text{Bi}_4\text{Pd}_3$  crystallizes in the cubic  $\text{Y}_3\text{Sb}_4\text{Au}_3$  phase of space group  $I\bar{4}3d$ , which is noncentrosymmetric and nonsymmorphic<sup>1</sup>, and preserves time reversal symmetry as evidenced by muon spin rotation<sup>2</sup>. It thus fulfills the necessary conditions to be a (nonmagnetic) Weyl semimetal. Indeed, density functional theory (DFT) identified a number of Weyl nodes in its electronic structure, albeit more than 100 meV away from the Fermi energy<sup>2</sup>. This is consistent with the expectation that even though DFT cannot capture the correlation physics, it does reflect the symmetry constraints.

Furthermore,  $\text{Ce}_3\text{Bi}_4\text{Pd}_3$  is a heavy fermion compound with a single ion Kondo temperature of 13 K as estimated from specific heat<sup>1</sup>. It becomes fully Kondo coherent only below about 3 K as shown by a magnetoresistance analysis<sup>1</sup>. As the temperature is lowered into the Kondo coherent regime, the material—still governed by the same space-group constraint—hosts Kondo-generated heavy Weyl quasiparticles, with Weyl nodes near the Fermi energy.

There are two key signatures of Weyl-Kondo nodes in the Kondo coherent state: (i) a giant spontaneous (zero field) Hall effect and an associated (equally giant) even-in-field continuation of it in finite fields (Fig. 1e), and (ii) an electronic specific heat coefficient  $\Delta C/T$  that is linear in  $T^2$ , i.e.  $\Delta C/T = \Gamma T^2$ , and is associated with the linear dispersion of the Weyl nodes (Fig. 1f).



Both emerge only in the Kondo coherent state<sup>1,2</sup> and are thus clearly Kondo driven. The giant magnitude of the spontaneous Hall effect was attributed to Weyl nodes—where the Berry curvature diverges—being essentially pinned to the Fermi energy<sup>2</sup>. The giant value of the slope  $\Gamma$  reveals that the Weyl quasiparticles have velocities  $v^*$  that are renormalized by three orders of magnitude with respect to values typical for noninteracting Weyl or Dirac semimetals (as shown in<sup>1,3</sup>,  $\Gamma \propto (1/v^*)^3$ ). Thus, the Kondo interaction appears to create—from the Weyl nodes present in the noninteracting bandstructure—extremely flat Weyl-Kondo cones in the immediate vicinity to the Fermi level, which is commensurate with theoretical expectations for a pertinent model<sup>3</sup>.

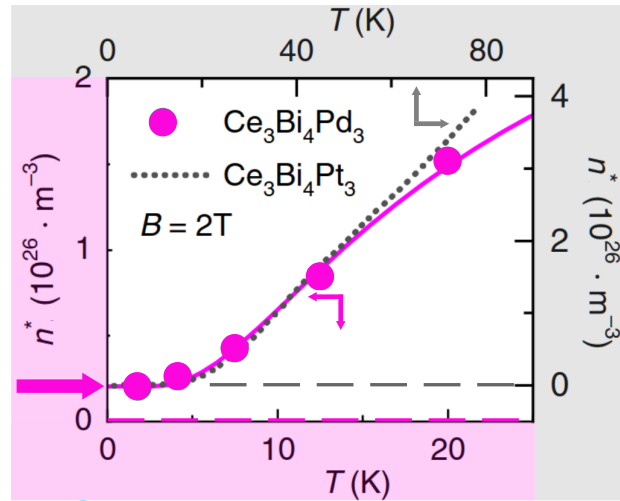
The spontaneous Hall effect was also shown to have nonlinear current-voltage characteristics and to display a second harmonic response under AC current drive<sup>2</sup>. Other contributions such as contact misalignment<sup>2</sup>, skew scattering (Supplementary Note 8), or multiband effects (Supplementary Note 9) were ruled out to play any significant role (see also Ref. <sup>2</sup>). Also spurious extrinsic effects can be discarded because (i) the spontaneous Hall effect is reproducible from sample to sample (Fig. S8 of Ref. <sup>2</sup>), (ii) it exhibits a systematic Hall angle dependence (Fig. S9 of Ref. <sup>2</sup>), (iii) nonlinear-in-current DC, as well as  $0\omega$  and  $2\omega$  AC contributions occur as expected and set in at the same temperature (Figs. 2D-F, S6, S7 and Table S1 of Ref. <sup>2</sup>), and (iv) the spontaneous Hall signal emerges as the material becomes Kondo coherent (Fig. 1D of Ref. <sup>2</sup>).

Two comments are due: Firstly, because the Weyl bands of  $\text{Ce}_3\text{Bi}_4\text{Pd}_3$  are flat bands (renormalized by three orders of magnitude compared to the noninteracting case), ARPES lacks the resolution needed to resolve them. The linear dispersion is instead detected by  $\Delta C/T \propto T^2$  (see above). Secondly, magnetotransport signatures of the chiral anomaly are expected to be suppressed by the strongly reduced quasiparticle velocities (equally by three orders of magnitude compared to the noninteracting case). The spontaneous Hall effect plays the analogous role in that it probes the Berry curvature distribution.

Both above-mentioned key signatures (i and ii), as well as an associated third one, an odd-in-field anomalous Hall effect (Fig. 1d and Supplementary Fig. 6 top row), are successively suppressed with increasing magnetic field (Fig. 1d-f) and vanish, in the  $T = 0$  limit, at a critical field  $B_{c1}$  (Fig. 4a, red symbols).

## Supplementary Note 2: Semimetallic ground state of $\text{Ce}_3\text{Bi}_4\text{Pd}_3$ in zero magnetic field

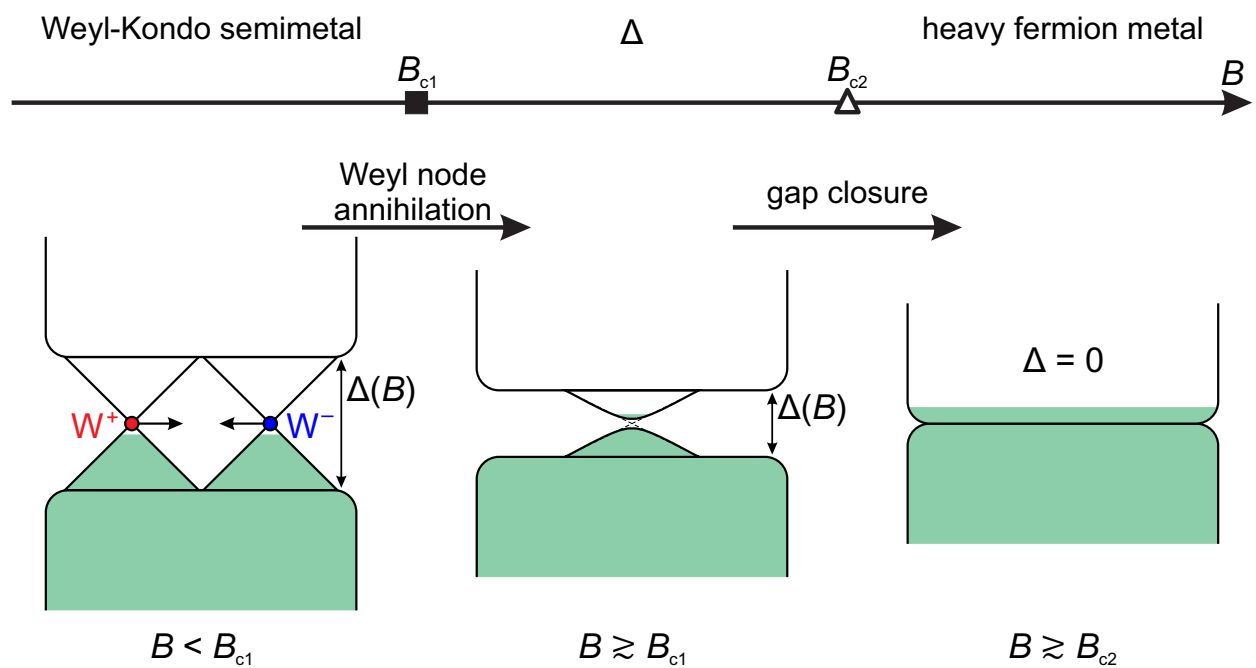
In zero magnetic field,  $\text{Ce}_3\text{Bi}_4\text{Pd}_3$  is a Weyl-Kondo semimetal<sup>2</sup>. The semimetallic nature of the ground state is also evidenced by the temperature dependence of the normal Hall coefficient  $R_H$  (the slope of the linear-in-field contribution to the antisymmetrized Hall resistivity, see Supplementary Note 7), which saturates at low temperatures to a constant value (see Fig. 1b and  $\tilde{R}_0$  in Fig. 2d). In a simple one-band model,  $R_H$  is inversely proportional to the charge carrier concentration  $n$ . A saturating  $R_H$  thus corresponds to a saturating  $n$ . In view of the small value of  $n$  (of the order of  $10^{26} \text{ m}^{-3}$ ), this is a characteristic of a semimetal. Note that this behavior is also seen in the  $\text{Ce}_3\text{Bi}_4\text{Pd}_3$  sample studied in<sup>4</sup> (Supplementary Fig. 1), even though an insulating ground state is claimed in that work.



**Supplementary Fig. 1: Temperature-dependent charge carrier concentrations of  $\text{Ce}_3\text{Bi}_4\text{Pd}_3$  and  $\text{Ce}_3\text{Bi}_4\text{Pt}_3$ .** Charge carrier concentration  $n^*$  of  $\text{Ce}_3\text{Bi}_4\text{Pd}_3$  (pink, bottom and left axes) and of  $\text{Ce}_3\text{Bi}_4\text{Pt}_3$  (grey, top and right axes), as extracted from the (antisymmetrized) Hall resistivity at 2 T in a one-band model. For  $\text{Ce}_3\text{Bi}_4\text{Pd}_3$ ,  $n^*$  saturates to a finite value in the low-temperature limit (pink arrow), consistent with a semimetallic ground state. By extension, the Hall coefficient is not thermally activated in the relevant low-temperature regime. For  $\text{Ce}_3\text{Bi}_4\text{Pt}_3$ , by contrast,  $n^*$  saturates to zero (on this linear scale), consistent with the Kondo insulating ground state of this compound. Figure adapted from<sup>4</sup>.

### Supplementary Note 3: Cartoon of the correlated bandstructure of $\text{Ce}_3\text{Bi}_4\text{Pd}_3$ under magnetic field tuning

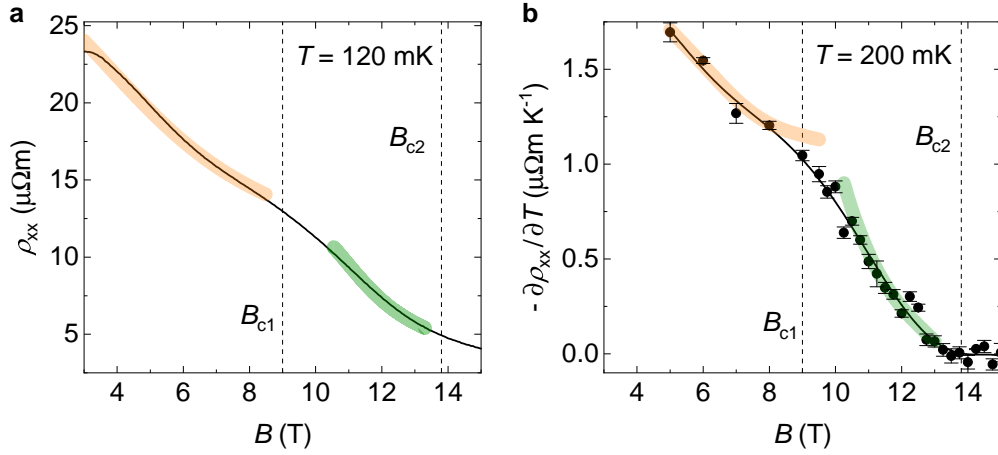
Taking all results of the present work together allows us to draw a cartoon of how the correlated electronic bandstructure of  $\text{Ce}_3\text{Bi}_4\text{Pd}_3$  changes under the action of the magnetic field (Supplementary Fig. 2). Note that this is a strongly simplified sketch, which ignores realistic dispersions, the multiplicity of Weyl nodes etc. Ab initio-based many-body calculations will be needed to refine this picture.



**Supplementary Fig. 2: Cartoon of the correlated electronic bandstructure of  $\text{Ce}_3\text{Bi}_4\text{Pd}_3$  under magnetic field tuning.** At low fields, a Weyl ( $W^+$ ) and an anti-Weyl node ( $W^-$ ) are situated within a Kondo insulator gap [ $\Delta(B)$ ], slightly above the Fermi energy (the green shading represents the electron filling). The momentum-space separation between the nodes decreases with increasing magnetic field (arrows), but their energy is unchanged. At a first critical magnetic field ( $B_{c1}$ ), the Weyl nodes meet in momentum space and annihilate, which gaps out the Weyl dispersion. At a second critical magnetic field ( $B_{c2}$ ), the Kondo insulator gap is closed and the system becomes a heavy fermion metal.

#### Supplementary Note 4: Evidence for a two-stage transition from electrical resistivity

As pointed out in the main text, the rather drastic features seen at  $B_{c1}$  and  $B_{c2}$  in the field-dependent Hall resistivity isotherms (Fig. 1c) leave clear signatures also in the temperature- and field-dependent electrical resistivity (Fig. 1a,c). In Supplementary Fig. 3a we show the relevant field range of  $\rho_{xx}(B)$  data at 120 mK. A rather pronounced change of the magnetoresistance character is observed at  $B_{c1}$ . The magnetoresistance of Kondo systems is typically negative and sizeable, in agreement with the broadened step-like resistance decrease obtained by Schlottmann from a Bethe-Ansatz solution of the Coqblin-Schrieffer model (“Schlottmann scaling”)<sup>5</sup>. Such behavior is seen both in the low-field range below  $B_{c1}$  and in the intermediate-field range between  $B_{c1}$  and  $B_{c2}$  (see shaded orange and green curves in Supplementary Fig. 3a). The “double decay” shape separated by  $B_{c1}$  naturally suggests that the magnetoresistance of  $\text{Ce}_3\text{Bi}_4\text{Pd}_3$  is governed by two different scales, one of the Weyl-Kondo semimetal below  $B_{c1}$  and one of the intermediate phase

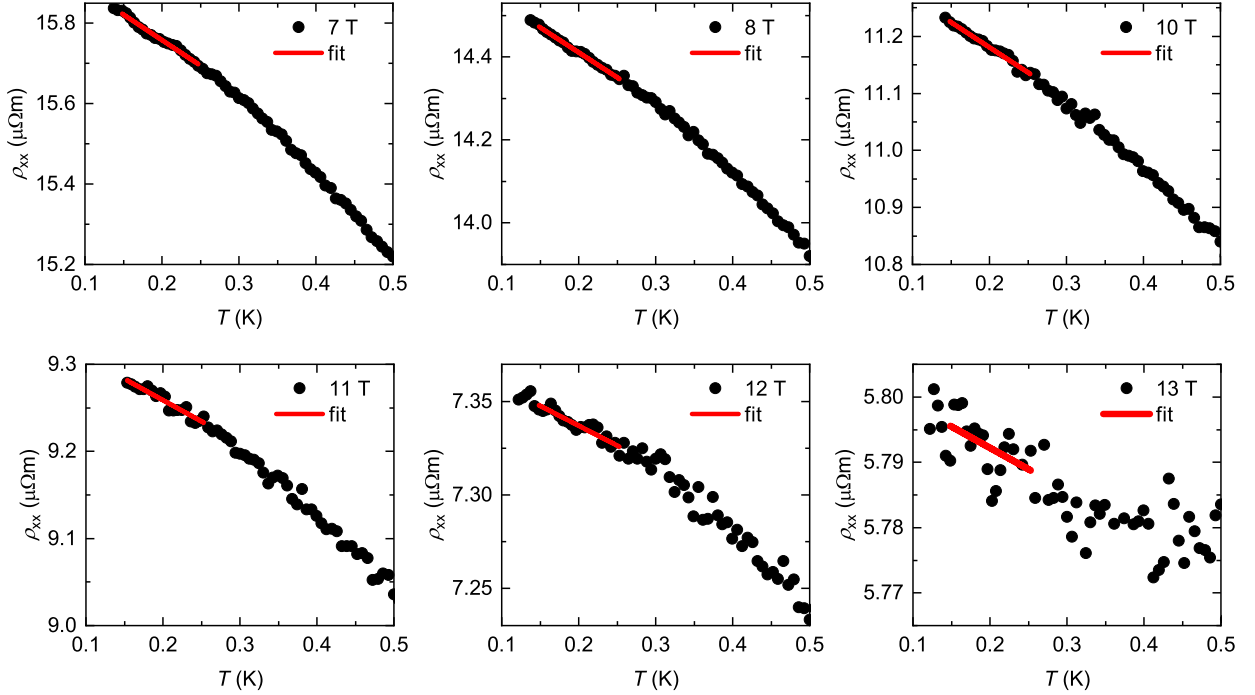


**Supplementary Fig. 3: Field-dependent electrical resistivity.** (a) Electrical resistivity vs magnetic field at 120 mK, together with Schlottmann fits<sup>5</sup> (see text). Their purpose is solely to indicate what type of magnetoresistance might be expected in a Kondo system. It is clear that the entire curve cannot be attributed to a Kondo system with a single energy scale. (b) Temperature derivatives (full symbols) of iso-field  $\rho_{xx}(T)$  curves, taken at 200 mK, defined as the slopes of the linear fits in Supplementary Fig. 4. The error bars represent the standard errors of the slopes of these fits. The lines are guides to the eyes (they have also Schlottmann shape, see shaded lines).

Signatures at the critical fields  $B_{c1}$  and  $B_{c2}$  are clearly revealed.



between  $B_{c1}$  and  $B_{c2}$ . The signature at  $B_{c2}$  is more pronounced in iso-field  $\rho_{xx}(T)$  curves, as shown next. In Supplementary Fig. 3b we plot the temperature derivative of these curves, taken at 200 mK, vs magnetic field (see Supplementary Fig. 4 for how the derivatives were obtained). Here, not only the transition at  $B_{c1}$  is clearly resolved, but also that at  $B_{c2}$ . To conclude, the field- and temperature-dependent electrical resistivity, with clear signatures at  $B_{c1}$  and  $B_{c2}$ , underpins the presence of the three phases discussed in the main text.



**Supplementary Fig. 4: Temperature dependent iso-field electrical resistivity curves.** The red lines are linear fits to the data (full symbols) in the range  $(200 \pm 50)$  mK. Their slopes correspond to the local derivative of  $\rho(T)$  at 200 mK and are plotted vs field in Supplementary Fig. 3.

#### Supplementary Note 5: Specific heat

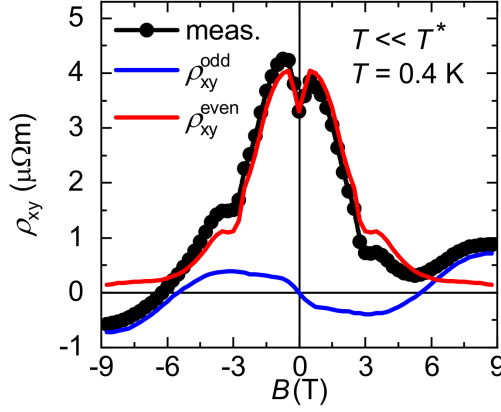
In a Weyl-Kondo semimetal, the electronic contribution to the temperature-dependent specific heat varies as  $C = \Gamma T^3$ , with  $\Gamma = 7\pi^2 k_B^2 / (\hbar v^*)^3$  (Ref. <sup>3</sup>), as experimentally observed in  $\text{Ce}_3\text{Bi}_4\text{Pd}_3$  (Ref. <sup>1</sup>). The strongly renormalized quasiparticle velocity  $v^*$  boosts the electronic  $\Gamma T^3$  term to the point that it even overshoots the Debye  $\beta T^3$  term of the lattice<sup>1</sup>.

To track the evolution of the Weyl-Kondo semimetal phase in  $\text{Ce}_3\text{Bi}_4\text{Pd}_3$  with magnetic field,

we measured the temperature dependent specific heat  $C_{\text{Ce}}(T)$  of the compound at several fixed magnetic fields. In a first step, we determine the electronic contribution to the measured data by subtracting the specific heat  $C_{\text{La}}(T)$  of the nonmagnetic reference compound  $\text{La}_3\text{Bi}_4\text{Pd}_3$ . In a second step, to isolate the temperature-dependent part, we subtract a trivial Sommerfeld offset  $\gamma$  in the  $(C_{\text{Ce}} - C_{\text{La}})/T$  data of  $\gamma = 209 \text{ mJ}/(\text{mol-Ce K}^2)$ , which is in good agreement with  $\gamma = 200 \text{ mJ}/(\text{mol-Ce K}^2)$  measured elsewhere<sup>1</sup>. We observe that the  $\Delta C/T = \Gamma T^2$  behavior seen at  $B = 0$  is successively suppressed with increasing magnetic field, until it is no longer discernible for  $B = 9 \text{ T}$  (Fig. 1f).

### Supplementary Note 6: Even-in-field Hall resistivity

As discussed in Ref.<sup>2</sup> and summarized in Supplementary Note 1, the spontaneous Hall effect is the key signature of a Weyl-Kondo semimetal in zero magnetic field. In finite magnetic field, it finds continuation in an even-in-field contribution  $\rho_{xy}^{\text{even}}(B)$  (Supplementary Fig. 5), that can be obtained by symmetrizing the Hall resistivity (after eliminating contact misalignment contributions, see Supplementary Information Sect. I of Ref.<sup>2</sup>).  $\rho_{xy}^{\text{even}}(B)$  cannot be induced by the magnetic field. Instead, it is—just as the spontaneous Hall effect—due to the odd-in-momentum Berry curvature divergences at the Weyl nodes of a TRS preserving (nonmagnetic) Weyl semimetal. As this contribution cannot be confused with any other Hall contribution (such as multiband effects, magnetization-related anomalous Hall effect, etc., see Supplementary Information Sect. I of Ref.<sup>2</sup>), it is the key signature of the Weyl-Kondo semimetal in finite magnetic field. The role of the magnetic field is to tune the Weyl-Kondo semimetal phase and ultimately suppress it, thereby consecutively weakening  $\rho_{xy}^{\text{even}}(B)$  and finally suppressing it as the Weyl nodes annihilate, as shown in Fig. 1e and discussed in the main text.



**Supplementary Fig. 5: Hall resistivity of  $\text{Ce}_3\text{Bi}_4\text{Pd}_3$  at 0.4 K.** The magnetic field-dependent DC Hall resistivity  $\rho_{xy}(B)$  consists of an odd-in- $B$  ( $\rho_{xy}^{\text{odd}}(B)$ , blue) and an even-in- $B$  ( $\rho_{xy}^{\text{even}}(B)$ , red) component. The former is “normal” in the sense that it is induced by the magnetic field. It can be further decomposed into a linear-in-field normal Hall effect, and a nonlinear anomalous Hall effect induced by the time reversal symmetry (TRS)-breaking applied magnetic field. The even-in- $B$  component, which cannot be induced by the magnetic field, is the finite-field continuation of the spontaneous (zero field) Hall effect. It is due to the odd-in-momentum Berry curvature divergences at the Weyl nodes of a TRS preserving (nonmagnetic) Weyl semimetal. As this contribution cannot be confused with any other Hall contribution (such as multiband effects, magnetization-related anomalous Hall effect, etc.), it is the key signature of the Weyl-Kondo semimetal. From Ref.<sup>2</sup>.

### Supplementary Note 7: Analysis of the normal Hall resistivity data

In the linear response sense, the Hall coefficient  $R_H$  is defined as the initial slope of the Hall resistivity  $\rho_{xy}(B)$ , i.e.,  $R_H = \lim_{B \rightarrow 0} \partial \rho_{xy}(B) / \partial B$ . In the case of a driving magnetic field  $B_0$ , it may still be defined as  $R_H(B_0) = \partial \rho_{xy}(B) / \partial B$  at  $B = B_0$ . In heavy fermion systems that undergo a magnetic field-tuned quantum phase transition, it has been experimentally demonstrated by cross-field experiments that it is the local derivative  $\partial \rho_{xy}(B) / \partial B$  that corresponds to the Hall coefficient<sup>6,7</sup>.

In experiments where a magnetic field simultaneously drives the phase transition and is used to measure the Hall resistivity,  $R_H(B)$  follows a step-like function that sharpens as the temperature

is lowered, and can be fitted with a function

$$R_H(B) = R_\infty - (R_\infty - R_0) \left[ 1 + \left( \frac{B}{B^*} \right)^p \right]^{-1} \quad (1)$$

where  $R_0$  and  $R_\infty$  are the Hall coefficients of the initial ( $B \rightarrow 0$ ) and final phases ( $B \rightarrow \infty$ ), respectively,  $B^*$  is the magnetic field at the transition, and  $p$  is associated with the width of the transition. The total Hall resistivity is then given by

$$\rho_{xy} = \int R_H(B) dB. \quad (2)$$

The Hall resistivity of  $\text{Ce}_3\text{Bi}_4\text{Pd}_3$  (Fig. 1c) has two-step nature; therefore three phases must be considered (low field: 0; intermediate field: 1; high field: 2), each with a constant Hall coefficient ( $R_0$ ,  $R_1$ , and  $R_2$ ) defined as the field derivative of the Hall resistivity  $\rho_{xy}(B)$ . The total fitting function concatenates the information from the slopes of  $\rho_{xy}(B)$  from each phase, resulting in the fitting function

$$R_H(B) = R_2 - (R_2 - R_{H,1}) \left[ 1 + \left( \frac{B}{B_2^*} \right)^{p_2} \right]^{-1} \quad (3)$$

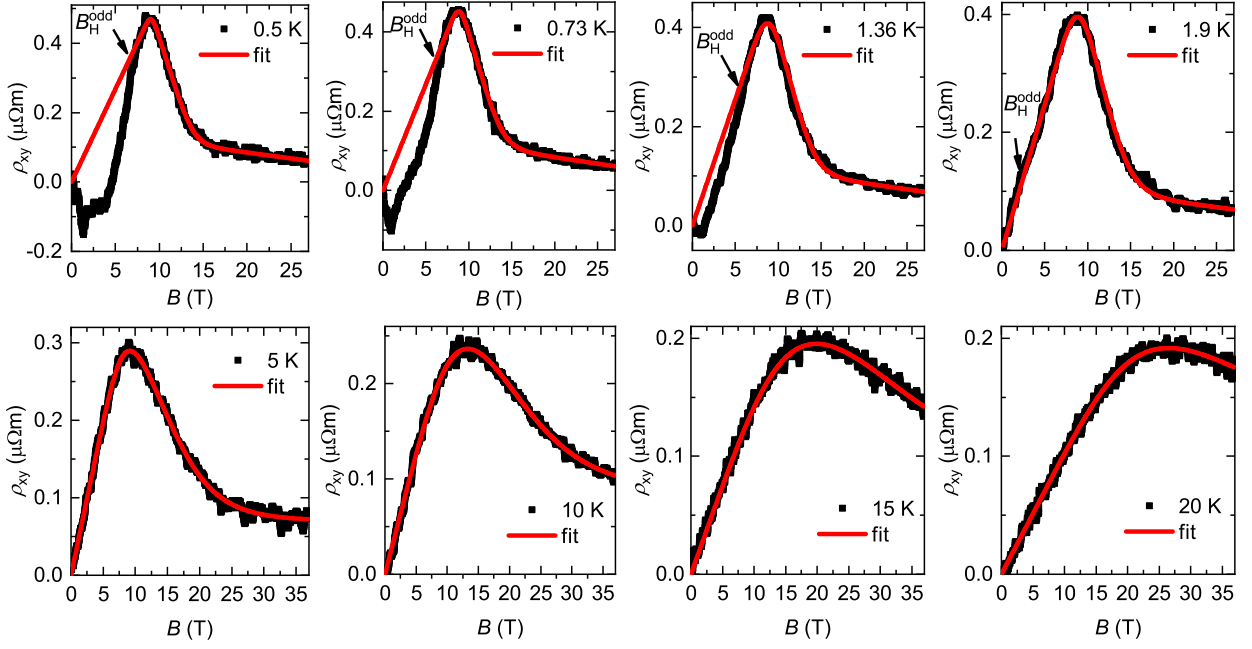
where

$$R_{H,1}(B) = R_1 - (R_1 - R_0) \left[ 1 + \left( \frac{B}{B_1^*} \right)^{p_1} \right]^{-1}. \quad (4)$$

The characteristic widths of the transitions between consecutive phases ( $\Delta B_1$  and  $\Delta B_2$ ) correspond to the full width at half maximum (FWHM) of the second derivatives of the calculated  $\rho_{xy}(B)$  curves.

Fits at two selected temperatures are shown in the main part (Fig. 2a,b). Further fits are shown in Supplementary Fig. 6. All parameters obtained from these fits are displayed in Fig. 2c-f.

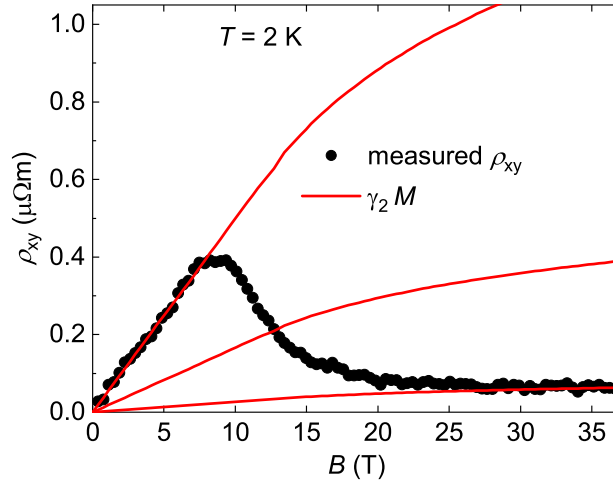




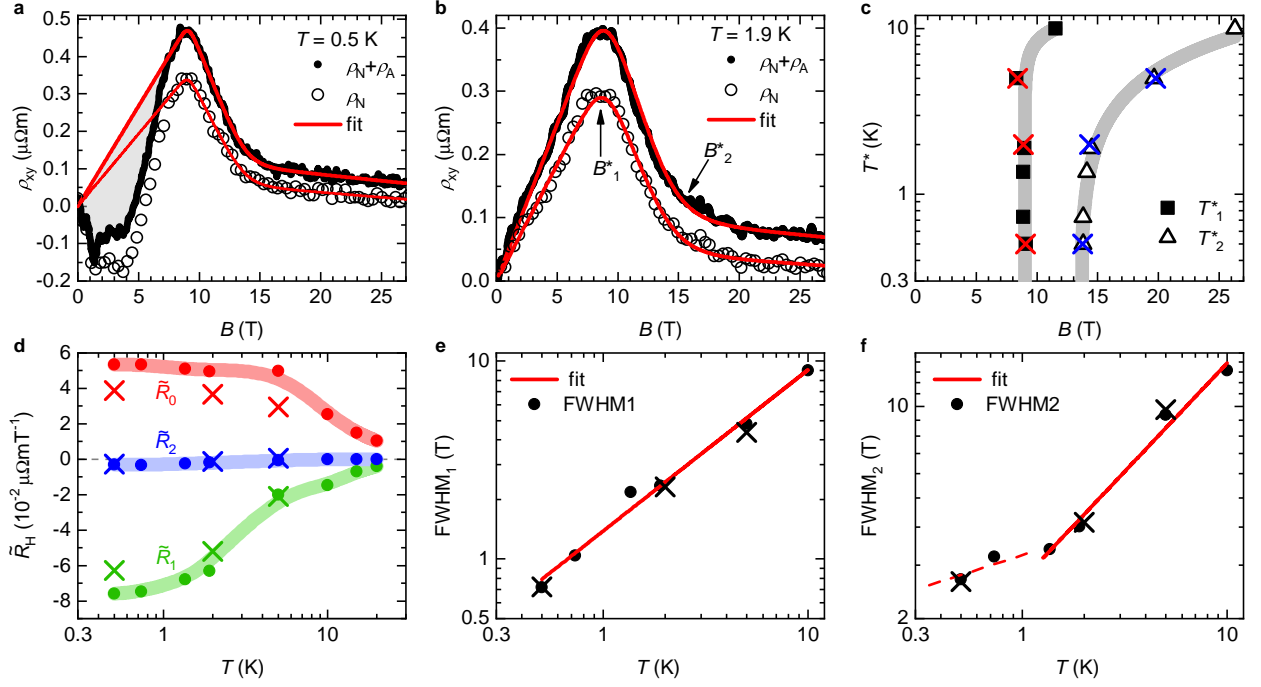
**Supplementary Fig. 6: Two-stage crossover fits to the Hall resistivity.** Hall resistivity data for various temperatures between 0.5 and 20 K (black symbols), and the corresponding two-stage transition fits (red lines) using Supplementary Eqs. (1-4). Below 1.36 K, the fit range is between 8.4 and 27 T, to avoid influence of the Berry curvature-related (odd-in- $B$ ) anomalous Hall effect (negative contribution superimposed to the linear-in- $B$  normal Hall effect discussed also in Ref. <sup>2</sup>). Arrows indicate the field  $B_{\text{H}}^{\text{odd}}$  above which the deviation from the initial linear behavior (red line) drops below 5 %. These fields are plotted as temperature scales  $T_{\text{H}}^{\text{odd}}(B)$  in Fig. 4a. With increasing temperature, the crossovers broaden and move to higher fields. Thus, at 5 K and above, fits were done up to 37 T to capture as much of the crossover behavior as possible. At 15 K and above, the second transition has moved out of the measured magnetic field range, and thus a two-stage crossover fit loses meaning. All fitted parameters are displayed in Fig. 2c-f.

### Supplementary Note 8: Anomalous Hall effect

Heavy fermion compounds in their Kondo incoherent regime at elevated temperatures frequently exhibit a significant anomalous Hall signal due to skew scattering<sup>8</sup>. In the Kondo coherent regime at low temperatures, by contrast, this contribution is known to become very small<sup>6,8,9</sup>. The skew scattering-driven anomalous Hall effect is frequently estimated by  $\rho_A(B) \sim \rho(B)M(B)$  (Ref.<sup>8</sup>). This is, however, only valid if the field dependence of  $\rho$  is dominated by that of the scattering time<sup>10</sup>. If the Fermi surface undergoes an abrupt change, as is the case in the Kondo destruction scenario of heavy fermion metals<sup>6</sup> and as we observe here for  $\text{Ce}_3\text{Bi}_4\text{Pd}_3$  at  $B_{c1}$  and  $B_{c2}$ , the field dependence of  $\rho$  may be dominated by that of the charge carrier concentration. In this situation, the expression  $\rho_A(B) \sim M(B)$  (Refs.<sup>11,12</sup>) is more appropriate. Thus, in Supplementary Fig. 7, we plot  $\rho_{xy}(B)$  together with the magnetization  $M(B)$  (Ref.<sup>4</sup>), scaled by  $\gamma_2$  to fit  $\rho_{xy}(B)$  at low ( $B < B_{c1}$ ), intermediate ( $B_{c1} < B < B_{c2}$ ), and high ( $B > B_{c2}$ ) fields. It is clear that none of the characteristic features of  $\rho_{xy}(B)$  is seen in  $M(B)$ . Thus, skew scattering is not the cause of the observed magnetic field dependence of  $\rho_{xy}$  in  $\text{Ce}_3\text{Bi}_4\text{Pd}_3$ .



**Supplementary Fig. 7: Estimation of skew scattering contribution to Hall effect from magnetization.** Field-dependent Hall resistivity at 2 K, together with magnetization data at 1.5 K taken from Ref.<sup>4</sup> and scaled by  $\gamma_2$  to match  $\rho_{xy}$  at low, intermediate, and high fields (see text). The fact that  $\gamma_2 M(B)$  does not reproduce the shape of  $\rho_{xy}(B)$  reveals that the anomalous Hall effect due to skew scattering is unimportant in  $\text{Ce}_3\text{Bi}_4\text{Pd}_3$ .



**Supplementary Fig. 8: Estimation of skew scattering contribution to Hall effect from magnetization and electrical resistivity.** Analysis of the two-crossover behavior as presented in Fig. 2, redone under the (unrealistic, see text) assumptions that, firstly, the field dependence of the electrical resistivity is due to skew scattering only and that thus the anomalous Hall effect is given by  $\rho_A(B) = \gamma_2 \rho(B) M(B)$  and that, secondly, the prefactor  $\gamma_2$  assumes the maximum possible value. **(a,b)** As-measured Hall resistivity isotherms (full black points) and data with the (hypothetical) skew scattering contribution  $\rho_A$  subtracted (open symbols), along with the respective two-transition fits. **(c-f)** Fit parameters obtained for the as-measured (full circles) and (hypothetical) skew scattering corrected data (crosses). The fact that the key fit parameters quantifying the crossovers ( $T^*$  and FWHM) are essentially unchanged shows that even the maximum estimated anomalous Hall contribution does not have any appreciable effect on the Hall crossovers.

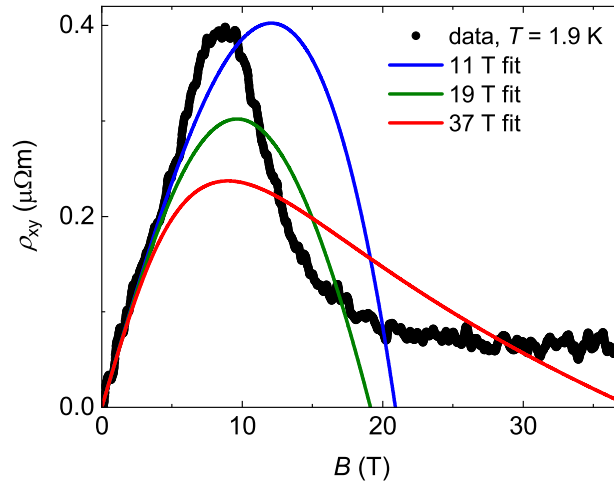
In the next step we ignore the above conclusion and nevertheless use  $\rho_A(B) = \gamma \rho(B) M(B)$  (Ref. <sup>8</sup>) as an estimate of the absolute maximum skew scattering contribution. We furthermore use  $\gamma = 0.08 \text{ K/T}$  ( $\gamma = 0.05 \text{ Ce}/\mu_B$  when  $M$  is in units of  $\mu_B/\text{Ce}$ ), which is the upper limit for Ce-based heavy fermion materials<sup>8</sup>. We then subtract  $\rho_A(B)$  from our data and redo the two-crossover fit at several representative temperatures (Supplementary Fig. 8). The results show that

the skew scattering contribution to the initial Hall coefficient is at most  $\sim 20\%$  (Supplementary Fig. 8d). Importantly, neither the crossover positions nor their widths change considerably (Supplementary Fig. 8c,e-f). We conclude that even in the unlikely event that skew scattering is present in the  $\rho_{xy}(B)$  data this would not contribute appreciably to the crossover behavior observed in  $\text{Ce}_3\text{Bi}_4\text{Pd}_3$ .

### Supplementary Note 9: Hall effect from multiple bands

To investigate whether the pronounced nonlinearity of the Hall resistivity  $\rho_{xy}(B)$  might, alternatively, be a multiple band effect, we have performed an effective two-band analysis using a recently established robust scheme<sup>13</sup>. We perform the analysis on a representative  $\rho_{xy}(B)$  curve at  $T = 1.9$  K, in three different fit ranges (see Supplementary Fig. 9), to test up to which field a two-band model can capture the observed behavior. All fit parameters are given in Supplementary Table 1.

We see that even the fit up to 11 T has very poor quality, showing that a two-band model cannot reproduce the sharp bending at  $B_{c1}$ . Also the parameters obtained for this fit (one electron and



**Supplementary Fig. 9: Estimation of contribution to Hall effect from multiband effects.**

Two-band analysis of the Hall resistivity vs field isotherm of  $\text{Ce}_3\text{Bi}_4\text{Pd}_3$  at 1.9 K, using the robust analysis scheme of Ref.<sup>13</sup>. The three curves represent fits from zero field up to 11, 19, and 37 T, respectively, to test whether in any of these field ranges the experimental  $\rho_{xy}(B)$  curve can be reproduced. The failure shows that the pronounced nonlinearity of  $\rho_{xy}(B)$  cannot be due to two-band (or multiband) effects.



Supplementary Table 1: Fit parameters for two-band analysis done in Supplementary Fig. 9. All values are rounded up to the first digit, and thus, must be regarded as approximate values. A positive (negative) sign of the mobility denotes a hole-like (electron-like) band.

parameters	11 T	19 T	37 T	unit
$n_1$	$9 \cdot 10^{23}$	$7 \cdot 10^{25}$	$1 \cdot 10^{27}$	$1/\text{m}^3$
$n_2$	$9 \cdot 10^{23}$	$1 \cdot 10^{24}$	$1 \cdot 10^{23}$	$1/\text{m}^3$
$\mu_1$	-2000	-40	-3	$\text{cm}^2/\text{Vs}$
$\mu_2$	2000	500	1000	$\text{cm}^2/\text{Vs}$

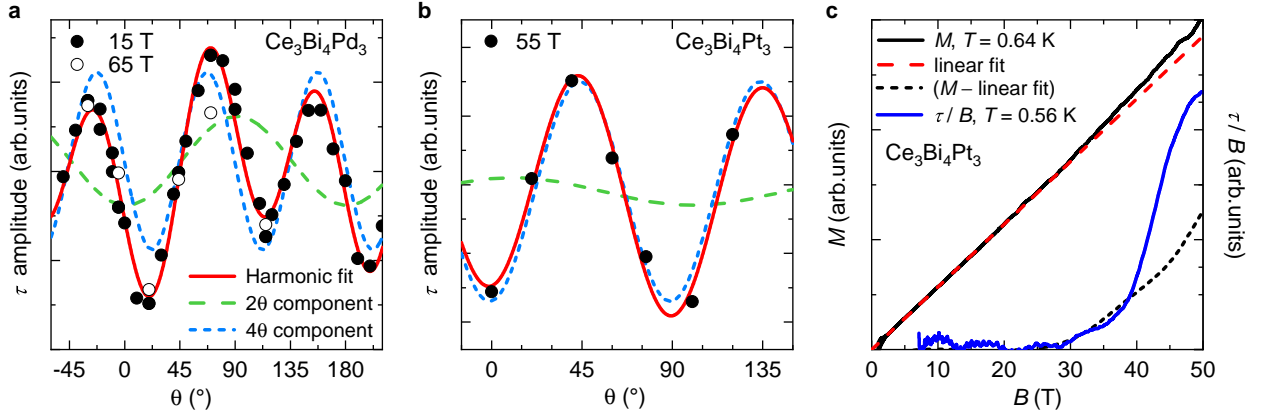
one hole band with  $|n_1| \approx |n_2| \approx 1 \times 10^{18} \text{ cm}^{-3}$ ,  $|\mu_1| \approx |\mu_2| \approx 2000 \text{ cm}^2/\text{Vs}$ ) appear rather unrealistic. Extending the field range does not bring any improvement. Thus, we conclude that it is highly unlikely that the observed nonlinearity is due to two- or multiband effects (even in the generic multiband situation, frequently two bands are found to dominate). The fact that the feature in  $\rho_{xy}(B)$  at  $B_{c1}$  coincides with the anomalies in  $\rho_{xx}(B)$  and  $\partial\rho_{xx}/\partial T(B)$  (Supplementary Fig. 3B) as well as with all other temperature scales reported in Fig. 4a supports, instead, that it is due to a crossover between phases with different Fermi volume.

### Supplementary Note 10: Analysis of torque magnetometry data

Angular-dependent magnetic torque measurements were obtained for  $\text{Ce}_3\text{Bi}_4\text{Pd}_3$  and  $\text{Ce}_3\text{Bi}_4\text{Pt}_3$  single crystals in pulsed fields up to 65 T at the NHMFL-LANL facility at Los Alamos. Piezoresistive levers of dimensions  $120 \mu\text{m} \times 50 \mu\text{m} \times 4 \mu\text{m}$  and unloaded resonant frequency of 250 to 300 kHz were used. In order to keep the response fast in the few ms of rising magnetic fields, small samples were cut from previously characterized single crystals, resulting in the loss of the crystallographic alignment.

For cubic, magnetically isotropic materials, a linear magnetization results in zero magnetic torque<sup>14</sup>. Indeed, a sizable torque signal develops in  $\text{Ce}_3\text{Bi}_4\text{Pd}_3$  and  $\text{Ce}_3\text{Bi}_4\text{Pt}_3$  only near the characteristic fields  $B_\tau$  (Fig. 3c,d). The angular dependence of the amplitude of the torque signal obtained at 0.5 K is displayed in Supplementary Fig. 10a for  $\text{Ce}_3\text{Bi}_4\text{Pd}_3$  and Supplementary Fig. 10b for  $\text{Ce}_3\text{Bi}_4\text{Pt}_3$ . For both compounds we found that the magnetic torque anisotropy is dominated by

a  $\sin(4\Theta + \alpha)$  component, as expected for magnetically anisotropic systems with cubic symmetry<sup>15</sup>. For  $\text{Ce}_3\text{Bi}_4\text{Pd}_3$ , the lower characteristic magnetic energy scale allowed us to obtain a large set of data points in pulsed fields up to 15 T (black dots). Full 65 T shots were performed then for selected angles (white dots). For this case, the angular dependence can be described by a superposition of a  $4\Theta$  and a  $2\Theta$  components, the former twice as large than the latter (ratio  $4\Theta/2\Theta \sim 2$ ). We attribute the smaller  $2\Theta$  component to shape anisotropy effects<sup>15</sup>.



**Supplementary Fig. 10: Torque magnetometry of  $\text{Ce}_3\text{Bi}_4\text{Pd}_3$  and  $\text{Ce}_3\text{Bi}_4\text{Pt}_3$ .** (a) Angular dependence of the torque signal of  $\text{Ce}_3\text{Bi}_4\text{Pd}_3$  at 0.5 K, obtained for magnetic field sweeps up to 15 T (black dots) and 65 T (white dots). The red solid line is the best fit to the 15 T data, and it corresponds to the superposition of a dominant  $4\Theta$  component (blue dotted line) and a smaller  $2\Theta$  contribution (green dashed line). (b) Similar data for  $\text{Ce}_3\text{Bi}_4\text{Pt}_3$ , with the torque amplitudes obtained at 55 T and 0.5 K. (c) High-field magnetization (black curve, left axis) and magnetic torque divided by applied magnetic field (blue curve, right axis) of  $\text{Ce}_3\text{Bi}_4\text{Pt}_3$  at 0.56 K. Above 30 T, the magnetization departs from linear-in- $B$  behavior (red dotted line, linear fit to the data below 30 T). The difference is plotted as black dotted curve on the right axis.

For  $\text{Ce}_3\text{Bi}_4\text{Pt}_3$ , the finite torque signal can only be accessed above 30 T. For this reason, fewer points of the angular dependence of the torque signal amplitude at 55 T are displayed in Supplementary Fig. 10b. Nevertheless, a good fit to the data can also be achieved with a superposition of  $4\Theta$  and  $2\Theta$  components ( $4\Theta/2\Theta \sim 8$ ). A full curve of magnetic torque divided by applied magnetic field is displayed in Supplementary Fig. 10c (blue solid line), alongside the measurement of magnetization obtained at a similar temperature (black solid line). Above 30 T, the magnetization

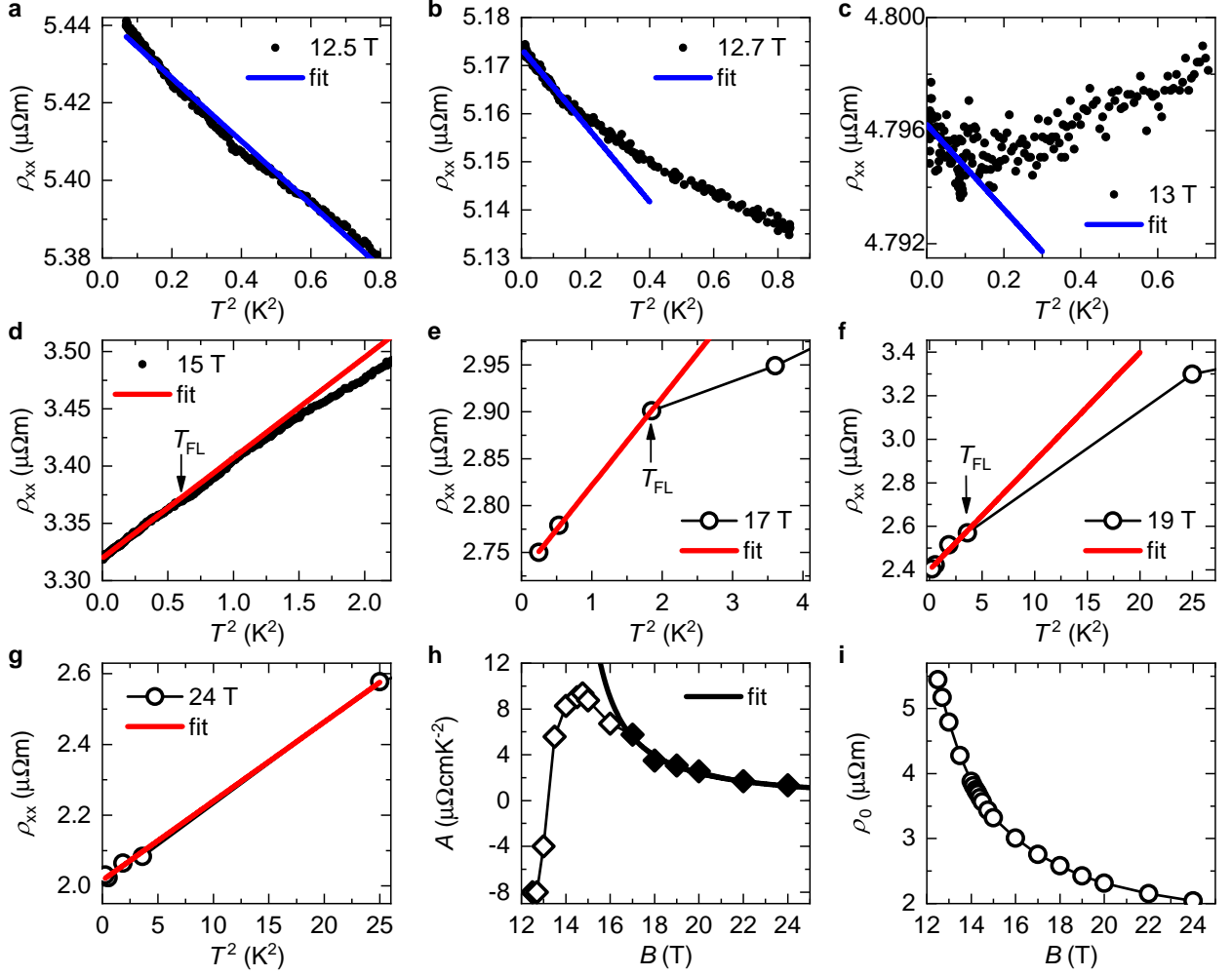
departs from linear-in- $B$  behavior (red dotted line, linear fit to the data below 30 T). The difference is plotted as a black dotted curve on the right axis. The onset of nonlinearity in  $M(B)$  thus coincides with the appearance of a sizeable torque signal.

### Supplementary Note 11: Fermi and non-Fermi liquid behavior

At high fields (sufficiently far above  $B_{c2}$ ) and low temperatures (below  $T_{FL}$ ) the electrical resistivity of  $\text{Ce}_3\text{Bi}_4\text{Pd}_3$  shows Fermi liquid behavior,  $\rho = \rho_0 + AT^2$ . This is evidenced by two sets of measurements: (i) iso-field temperature-dependent electrical resistivity measurements in a dilution refrigerator in fields up to  $B = 15$  T (Supplementary Fig. 11a-d), and (ii) isothermal magnetic field sweeps (Fig. 1b) taken at a high-field laboratory (Methods) and converted into iso-field temperature dependences in fields up to 24 T (Supplementary Fig. 11e-g). The residual resistivity  $\rho_0$  and the  $A$  coefficient extracted from fits to these data are shown in Supplementary Fig. 11h,i. Even at the largest field of 24 T, the  $A$  coefficient is still above  $1 \mu\Omega\text{cm}/\text{K}^2$ . Using the Kadowaki–Woods ratio  $A/\gamma^2 = 10^{-5} \mu\Omega\text{cm}(\text{mol K}/\text{mJ})^2$  this corresponds to a Sommerfeld coefficient of  $316 \text{ mJ}/(\text{mol K}^2)$ , which corresponds to a mass renormalization of at least 2 orders of magnitude. Thus, the Kondo effect is still at play. The influence of the Kondo insulating phase in the vicinity of  $B_{c2}$  on  $\rho(T)$  is discussed in the main text. It leads to a deviation from the divergence of the  $A$  coefficient indicated by the high-field data (Supplementary Fig. 11h, full line) and negative  $A$  values at  $B < B_{c2}$ . Also the continuous increase of the residual resistivity  $\rho_0$  with decreasing field across  $B_{c2}$  (Supplementary Fig. 11i) reflects a transition into a Kondo insulating phase.

To investigate whether the enhancement of the  $A$  coefficient upon approaching  $B_{c2}$  from the high-field side is due to a quantum critical point at  $B_{c2}$ , we measured the electrical resistivity at 15 T in the temperature range between 0.1 and 6 K (Fig. 3e, top and right axes). The measurement was done on a sample from the same batch as the sample of Supplementary Fig. 11 (and Fig. 3e, bottom and left axes, with residual resistivity  $\rho_0 \approx 4 \mu\Omega\text{m}$ ). Indeed, above the  $\rho_{xx} \sim T^2$  behavior at the lowest temperatures, we observe a non-Fermi liquid  $\rho_{xx} \sim T$  behavior, that persists up to  $T_{NFL} = 4.5$  K. This temperature is close to the Kondo coherence temperature (Ref. <sup>2</sup>). This is a sizeable range of non-Fermi liquid behavior which, as such, further supports the evidence for

quantum criticality.



**Supplementary Fig. 11: Analysis of Fermi liquid behavior in the electrical resistivity of  $\text{Ce}_3\text{Bi}_4\text{Pd}_3$ .** (a-g) Electrical resistivity data plotted vs  $T^2$  at various magnetic fields, with linear fits to determine the  $A$  coefficient, the residual resistivity  $\rho_0$ , and the onset temperature  $T_{\text{FL}}$ . (h)

$A$  coefficient vs applied magnetic field. The data above 16 T are well described by an

$A \propto (B - B_{c2})^{-p}$  law with  $B_{c2} = 13.8$  T and  $p = 0.985$ , suggesting that the effective mass

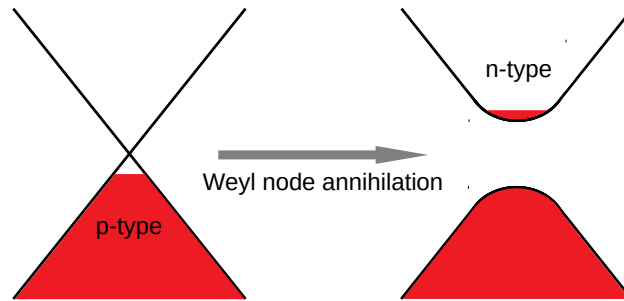
diverges at a quantum critical point situated at  $B_{c2}$ . Below 16 T, the  $A$  coefficient deviates from this behavior to lower values, which indicates that contributions from the Kondo insulating phase start to mix in. (i) Residual resistivity  $\rho_0$  vs applied magnetic field. The continued increase of  $\rho_0$

with decreasing field even below  $B_{c2}$  is attributed to the Kondo insulating phase.



### Supplementary Note 12: Sign change of Hall effect across Weyl node annihilation

Our experiments show that the (normal) differential Hall coefficient, which is the slope of the Hall resistivity isotherms (see Figs. 1d and 2a,b), changes sign at  $B_1^*$ . In the zero-temperature limit this change extrapolates to a discontinuous change (the FWHM vanishes in the  $T = 0$  limit, see Fig. 2e) of the charge carrier concentration from a positive to a somewhat smaller negative value (Fig. 4b, assuming a single band model). At this transition the topological response vanishes (Fig. 4a, red symbols), which we attribute to a Weyl node annihilation (main text and Supplementary Note 1). A simple sketch of this process illustrates that a sign change may occur rather naturally (Supplementary Fig. 12).



**Supplementary Fig. 12: Sketch of Weyl node gapping out.** When a Weyl and an anti-Weyl node meet in momentum space, they annihilate. This results in a gapping out of the nodes. The

sketch shows only one Weyl node before (left) and after (right) the annihilation. In the

Weyl-Kondo semimetal  $\text{Ce}_3\text{Bi}_4\text{Pd}_3$  the Fermi pocket (before annihilation) is tiny due to the pinning of the Weyl nodes to the immediate vicinity of the Fermi energy by the Kondo effect. As a result, even a small gap will change the sign of the Hall effect. Our experiments show that the Weyl quasiparticles are *p*-type (holes in the lower Weyl cone). As the gap opens at  $B_{c1}$ , the lower band gets completely filled and left-over carriers populate the upper band, thus changing the system from being *p*-type to *n*-type.

### Supplementary Note 13: Zeeman vs orbital effects of an applied magnetic field

The momentum space topology of electronic bands in crystalline solids depends on the material's symmetry, notably whether it preserves or breaks time reversal symmetry (TRS) and inversion symmetry (IS). The Weyl-Kondo semimetal  $\text{Ce}_3\text{Bi}_4\text{Pd}_3$  studied here breaks IS (via its noncen-

trosymmetric crystal structure) but preserves TRS (see Supplementary Note 1 and Ref.<sup>1</sup>). In materials that preserve both symmetries, the application of a magnetic field may break TRS and thereby change the topological state of the material.

Generally, a magnetic field acts on magnetic moments via the Zeeman effect and on moving electrical charge via the orbital effect. As such it is intuitive that in materials where local magnetic moments play an important role the Zeeman effect will dominate whereas in materials with highly mobile charge carriers the orbital effect will be most prominent.

We are interested here in the influence of an applied magnetic field on Dirac and Weyl semimetals. Because the Zeeman effect can break TRS it is of particular interest.

**Zeeman effect in noninteracting systems/systems without local moments.** We first discuss the noninteracting case, taking the Dirac semimetal  $\text{Cd}_3\text{As}_2$  as example. Using a combined DFT and effective low-energy model (based on  $k \cdot p$  perturbation theory) it was shown<sup>16</sup> that the material's Dirac node splits into four Weyl nodes (two with chirality  $\pm 1$  as commonly assumed and two additional ones with chirality  $\pm 2$ ). The effect is subtle: Even a huge effective Zeeman field of 100 T creates only a tiny  $k$ -space splitting (about 0.5% of the Brillouin zone size). Furthermore, the created Weyl nodes are not degenerate in energy. Thus, though frequently evoked, the magnetic-field induced formation of a Weyl semimetal from a Dirac semimetal is not straightforward. To achieve a Zeeman field of 100 T in pure  $\text{Cd}_3\text{As}_2$ , a material strongly dominated by orbital effects (see below), seems highly unrealistic. In fact, alternative ways—magnetic doping or proximity to a ferromagnet—have been considered to boost the spin-exchange field<sup>16,17</sup>.

**Zeeman effect in heavy fermion compounds.** In heavy fermion compounds, local magnetic moments are a natural ingredient of the system and thus a strong Zeeman effect does not need to be included artificially, as suggested in the Supporting Information of Ref.<sup>3</sup> and examined in Ref.<sup>18</sup>. In a Kondo lattice model for a simple nonsymmorphic and noncentrosymmetric crystal structure, the Zeeman effect was shown to move Weyl nodes—pinned to the Fermi energy—in momentum space until, at a continuous quantum phase transition, all Weyl nodes annihilate<sup>18</sup>. For the parameters selected in the model, this annihilation happens while the Kondo effect still operates.

**Orbital effect in noninteracting systems.** If Dirac points or Weyl nodes in noninteracting systems are situated near the Fermi energy (which may be achieved by doping), the low concentration of high-mobility carriers is expected to readily lead to quantum oscillations (just as in the case of clean topologically trivial semimetals). This has been seen in magnetotransport measurements of many noninteracting semimetals, both topological and topologically trivial. Some have been clearly evidenced to enter the quantum limit, where only the lowest Landau level is populated. The physics that may then happen is tunneling between left- and right-handed zeroth Landau levels, which is increasingly likely as the inverse magnetic length  $1/l_B = \sqrt{eB/\hbar}$ , a measure of the width of the zeroth Landau level wavefunction in momentum space, becomes of the order of the Weyl node separation. The wavefunctions of the Weyl and anti-Weyl quasiparticles then mix and the topological response is lost<sup>19</sup>. This process happens at a finite distance of the Weyl nodes in momentum space. As such it does not correspond to a Weyl node annihilation, which happens only if a Weyl and an anti-Weyl node meet in momentum space. Furthermore, as the momentum space width of the zeroth Landau level wavefunction increases (linearly) with field, one expects a crossover and not a (quantum) phase transition, clearly distinct from the situation observed in the present work for  $\text{Ce}_3\text{Bi}_4\text{Pd}_3$ .

Another point, emphasized in Ref. <sup>17</sup>, should also be noted. A large negative longitudinal magnetoresistance is a rather generic consequence of the quantum limit. It arises from the quenching of kinetic energy in the transverse directions and the associated suppression of backscattering in the effectively one-dimensional transport regime along the field direction. As concluded in Ref. <sup>17</sup>, it should therefore not be taken as evidence for the chiral anomaly and thus for Weyl physics.

**Orbital effect in heavy fermion compounds.** In heavy fermion compounds, the heavy quasiparticles primarily originate from the  $f$ -electron local moments. As such, their orbital coupling to an external magnetic field is strongly suppressed (and the Zeeman coupling dominates). Moreover, the mass renormalization via the Kondo effect leads to a renormalization of the effective carrier mobility by the same amount. In  $\text{Ce}_3\text{Bi}_4\text{Pd}_3$ , the Kondo temperature is 13 K<sup>1</sup>, about 1/1000th of a typical Fermi temperature in a noninteracting system. Thus, to reveal quantum oscillations in  $\text{Ce}_3\text{Bi}_4\text{Pd}_3$  would require a 1000-fold higher magnetic field than what is needed in a corresponding

noninteracting system. Note that the low mobilities of heavy fermion systems are a direct consequence of the extreme correlation strength and do not evidence enhanced disorder. Consistent with this expectation is our result that, even at the highest field of 65 T (and the lowest temperature of 0.43 K) we do not see signs of quantum oscillations (Fig. 3a). Thus, contributions of orbital effects on the topological quantum phase transition we observe at 9 T can be safely discarded.

#### **Supplementary Note 14: Comparison with weakly-interacting materials**

Weakly interacting Dirac and Weyl semimetals have been explored quite extensively. The purpose of this section is to help appreciate that they behave qualitatively differently from the strongly correlated Weyl-Kondo semimetal  $\text{Ce}_3\text{Bi}_4\text{Pd}_3$ . We first summarize the effect of magnetic field on two such systems as examples.

**( $\text{Pb}_{1-x}\text{Sn}_x$ ) $_{1-y}\text{In}_y\text{Te}$ .** In Ref. <sup>20</sup> evidence is reported for a topological metallic phase in ( $\text{Pb}_{1-x}\text{Sn}_x$ ) $_{1-y}\text{In}_y\text{Te}$  that persists over a finite pressure range.  $\text{Pb}_{0.75}\text{Sn}_{0.25}\text{Te}$  samples show an insulator–metal–insulator (I–M–I) transition as function of pressure (with the two critical pressures  $p_1$  and  $p_2$ ); in ( $\text{Pb}_{0.5}\text{Sn}_{0.5}$ ) $_{1-y}\text{In}_y$  samples only the first I–M transition (at  $p_1$ ) could be experimentally accessed. In the metallic (high mobility, very low carrier concentration) regime, quantum oscillations are seen, consistent with tiny Fermi pockets. As discussed above (Supplementary Note 13) this evidences the importance of the orbital magnetic field effect. When pressure is set close to the I–M transition but in the I phase, magnetic field can be used to tune the system into the metallic phase. This gives rise to large negative (transverse and longitudinal) magnetoresistance which, in conjecture with density functional theory (DFT) calculations, was interpreted as evidence for Weyl nodes. Whether the ferroelectric distortion, which is assumed in the DFT calculations but not resolved in the actual materials, and/or the Zeeman effect play significant roles in the proposed creation of Weyl nodes from Dirac points across  $p_1$  remains to be clarified. No data were yet provided for a Weyl node annihilation.

**TaAs and TaP.** In Ref. <sup>19</sup> high-field electrical resistivity measurements on TaAs are reported. At low fields (up to 7.5 T), quantum oscillations are visible. The approximate field independence of the resistivity  $\rho_{zz}$  (along the field direction, perpendicular to the Landau level quantization plane)

at intermediate fields is argued to evidence the chiral anomaly in a system with Weyl nodes and an inter-nodal scattering rate dominated by short-range impurity scattering. The increase of  $\rho_{zz}$  at even higher fields (around 50 T) is attributed to a gap formation due to the mixing of the left- and right-handed zeroth Landau level wavefunctions as described above (Supplementary Note 13). A simple tight-binding model for TaAs revealed<sup>19</sup> that the Zeeman effect is essentially negligible. Only for very large  $g$  factors (10), very large Weyl node separations ( $0.15\pi/a$ ), and very large fields (65 T) an appreciable effect (10%) on the gap size (opened by the orbital effect) is seen. In Ref.<sup>21</sup>, hysteretic behavior was observed at the quantum limit, but its origin remains to be clarified. In TaP the situation is very similar<sup>22</sup>, the only difference being that one pair of Weyl nodes in TaP remains ungapped up to the highest measured fields.

Also other (candidate) Dirac and Weyl semimetals show evidence for the dominance of orbital effects: the above discussed  $\text{Cd}_3\text{As}_2$ <sup>16,17</sup> (Supplementary Note 13), as well as  $\text{GdPtBi}$ <sup>23</sup>,  $\text{ZrTe}_5$ <sup>24,25</sup>,  $\text{ZrSiS}$ <sup>26</sup>, elemental  $\text{Te}$ <sup>27–29</sup>, etc.

Similar contrast between strongly correlated and weakly correlated topology also applies for other control parameters. For instance, in sequences considered to be driven by increasing spin-orbit coupling strength, a Weyl-Kondo semimetal to Kondo insulator transition was observed in  $\text{Ce}_3\text{Bi}_4(\text{Pd}_{1-x}\text{Pt}_x)_3$  with increasing  $x$ <sup>1</sup>, whereas in the series of weakly interacting compounds NbP – TaP – TaAs, ARPES could only detect a relatively modest change in Weyl node separation (by  $0.07 \text{ \AA}^{-1}$  across the whole series)<sup>30</sup>. The ability to continuously vary the magnetic field and thus the Zeeman coupling, as opposed to discrete steps in such substitution studies, was crucial for our investigation and makes this technique particularly powerful.

Another topic investigated are transitions between phases of different broken symmetry that, by consequence, also feature different topological properties. Examples are  $\text{CeSbTe}$ <sup>31</sup> and  $\text{Co}_3\text{Sn}_2\text{S}_2$ <sup>32,33</sup>. In the latter ARPES data together with DFT calculations were taken as evidence for Weyl nodes being present in the ferromagnetic state below the Curie temperature  $T_C = 176 \text{ K}$  but absent in the paramagnetic state above it<sup>32</sup>, and/or for Dirac loops above  $T_C$  and ferromagnetic Weyl loops below  $T_C$ <sup>33</sup>. In these cases, it is not the topological state as such that is controlled, but the topologically trivial “background” that changes from being paramagnetic to ferromagnetic as

temperature is lowered. This is distinct from the effect we have discovered here: a genuine Weyl node annihilation in a qualitatively unchanged background.

In summary, we are not aware of any published evidence for a genuine (Zeeman tuned) annihilation of Weyl nodes in a topological quantum phase transition.

## Supplementary References

1. Dzsaber, S., Prochaska, L., Sidorenko, A., Eguchi, G., Svagera, R., Waas, M., Prokofiev, A., Si, Q. & Paschen, S. Kondo insulator to semimetal transformation tuned by spin-orbit coupling. *Phys. Rev. Lett.* **118**, 246601 (2017).
2. Dzsaber, S., Yan, X., Eguchi, G., Prokofiev, A., Shiroka, T., Blaha, P., Rubel, O., Grefe, S. E., Lai, H.-H., Si, Q. & Paschen, S. Giant spontaneous Hall effect in a nonmagnetic Weyl-Kondo semimetal. *Proc. Natl. Acad. Sci. U.S.A.* **118**, e2013386118 (2021).
3. Lai, H.-H., Grefe, S. E., Paschen, S. & Si, Q. Weyl-Kondo semimetal in heavy-fermion systems. *Proc. Natl. Acad. Sci. U.S.A.* **115**, 93 (2018).
4. Kushwaha, S. K., Chan, M. K., Park, J., Thomas, S. M., Bauer, E. D., Thompson, J. D., Ronning, F., Rosa, P. F. S. & Harrison, N. Magnetic field-tuned Fermi liquid in a Kondo insulator. *Nat. Commun.* **10**, 5487 (2019).
5. Schlottmann, P. Bethe-Ansatz solution of the ground-state of the SU ( $2j + 1$ ) Kondo (Coqblin-Schrieffer) model: Magnetization, magnetoresistance and universality. *Z. Phys. B* **51**, 223 (1983).
6. Paschen, S., Lühmann, T., Wirth, S., Gegenwart, P., Trovarelli, O., Geibel, C., Steglich, F., Coleman, P. & Si, Q. Hall-effect evolution across a heavy-fermion quantum critical point. *Nature* **432**, 881 (2004).
7. Friedemann, S., Oeschler, N., Wirth, S., Krellner, C., Geibel, C., Steglich, F., Paschen, S., Kirchner, S. & Si, Q. Fermi-surface collapse and dynamical scaling near a quantum-critical point. *Proc. Natl. Acad. Sci. U.S.A.* **107**, 14547 (2010).
8. Fert, A. & Levy, P. M. Theory of the Hall effect in heavy-fermion compounds. *Phys. Rev. B* **36**, 1907 (1987).
9. Custers, J., Lorenzer, K., Müller, M., Prokofiev, A., Sidorenko, A., Winkler, H., Strydom, A. M., Shimura, Y., Sakakibara, T., Yu, R., Si, Q. & Paschen, S. Destruction of the Kondo effect in the cubic heavy-fermion compound  $\text{Ce}_3\text{Pd}_{20}\text{Si}_6$ . *Nat. Mater.* **11**, 189 (2012).



10. Nagaosa, N., Sinova, J., Onoda, S., MacDonald, A. H. & Ong, N. P. Anomalous Hall effect. *Rev. Mod. Phys.* **82**, 1539 (2010).
11. Arushanov, E., Kloc, C., Hohl, H. & Bucher, E. The Hall effect in  $\beta$ -FeSi<sub>2</sub> single crystals. *J. Appl. Phys.* **75**, 5106 (1994).
12. O'Handley, R. C. *The Hall effect and its applications*, Ed. C. L. Chien and C. R. Westgate (Plenum Press, New York, 1980).
13. Eguchi, G. & Paschen, S. Robust scheme for magnetotransport analysis in topological insulators. *Phys. Rev. B* **99**, 165128 (2019).
14. Michelutti, B. & Morin, P. Paramagnetic torque in cubic rare-earth compounds. *Phys. Rev. B* **46**, 14213 (1992).
15. Cullity, B. D. & Graham, C. D. *Introduction to Magnetic Materials*, 2nd Ed. (Wiley-IEEE Press, Hoboken, New Jersey, USA; ISBN 978-0-471-47741-9, 2009).
16. Baidya, S. & Vanderbilt, D. First-principles theory of the Dirac semimetal Cd<sub>3</sub>As<sub>2</sub> under Zeeman magnetic field. *Phys. Rev. B* **102**, 165115 (2020).
17. Burkov, A. A. & Balents, L. Weyl semimetal in a topological insulator multilayer. *Phys. Rev. Lett.* **107**, 127205 (2011).
18. Greife, S. E., Lai, H.-H., Paschen, S. & Si, Q. Extreme response of Weyl-Kondo semimetal to Zeeman coupling. *arXiv:2012.15841* (2020).
19. Ramshaw, B. J., Modic, K. A., Shekhter, A., Zhang, Y., Kim, E.-A., Moll, P. J. W., Bachmann, M. D., Chan, M. K., Betts, J. B., Balakirev, F., Migliori, A., Ghimire, N. J., Bauer, E. D., Ronning, F. & McDonald, R. D. Quantum limit transport and destruction of the Weyl nodes in TaAs. *Nat. Commun.* **9**, 2217 (2018).
20. Liang, T., Kushwaha, S., Kim, J., Gibson, Q., Lin, J., Kioussis, N., Cava, R. J. & Ong, N. P. A pressure-induced topological phase with large Berry curvature in Pb<sub>1-x</sub>Sn<sub>x</sub>Te. *Sci. Adv.* **3** (2017).
21. Zhang, Q. R., Zeng, B., Chiu, Y. C., Schönemann, R., Memaran, S., Zheng, W., Rhodes, D., Chen, K.-W., Besara, T., Sankar, R., Chou, F., McCandless, G. T., Chan, J. Y., Alidoust, N., Xu, S.-Y., Belopolski, I., Hasan, M. Z., Balakirev, F. F. & Balicas, L. Possible manifestations of the chiral anomaly and evidence for a magnetic field induced topological phase transition in the type-I Weyl semimetal TaAs. *Phys. Rev. B* **100**, 115138 (2019).
22. Zhang, C.-L., Xu, S.-Y., Wang, C. M., Lin, Z., Du, Z. Z., Guo, C., Lee, C.-C., Lu, H., Feng, Y., Huang, S.-M., Chang, G., Hsu, C.-H., Liu, H., Lin, H., Li, L., Zhang, C., Zhang, J., Xie, X.-C., Neupert, T.,

- Hasan, M. Z., Lu, H.-Z., Wang, J. & Jia, S. Magnetic-tunnelling-induced Weyl node annihilation in TaP. *Nat. Phys.* **13**, 979–986 (2017).
23. Hirschberger, M., Kushwaha, S., Wang, Z., Gibson, Q., Liang, S., Belvin, C. A., Bernevig, B. A., Cava, R. J. & Ong, N. P. The chiral anomaly and thermopower of Weyl fermions in the half-Heusler GdPtBi. *Nat. Mater.* **15**, 1161 (2016).
  24. Chen, R. Y., Chen, Z. G., Song, X.-Y., Schneeloch, J. A., Gu, G. D., Wang, F. & Wang, N. L. Magnetoinfrared spectroscopy of Landau levels and Zeeman splitting of three-dimensional massless Dirac fermions in ZrTe<sub>5</sub>. *Phys. Rev. Lett.* **115**, 176404 (2015).
  25. Zheng, G., Zhu, X., Liu, Y., Lu, J., Ning, W., Zhang, H., Gao, W., Han, Y., Yang, J., Du, H., Yang, K., Zhang, Y. & Tian, M. Field-induced topological phase transition from a three-dimensional Weyl semimetal to a two-dimensional massive Dirac metal in ZrTe<sub>5</sub>. *Phys. Rev. B* **96**, 121401 (2017).
  26. VanGennep, D., Paul, T. A., Yerger, C. W., Weir, S. T., Vohra, Y. K. & Hamlin, J. J. Possible pressure-induced topological quantum phase transition in the nodal line semimetal ZrSiS. *Phys. Rev. B* **99**, 085204 (2019).
  27. Hirayama, M., Okugawa, R., Ishibashi, S., Murakami, S. & Miyake, T. Weyl node and spin texture in trigonal tellurium and selenium. *Phys. Rev. Lett.* **114**, 206401 (2015).
  28. Ideue, T., Hirayama, M., Taiko, H., Takahashi, T., Murase, M., Miyake, T., Murakami, S., Sasagawa, T. & Iwasa, Y. Pressure-induced topological phase transition in noncentrosymmetric elemental tellurium. *Proc. Natl. Acad. Sci. U.S.A.* **116**, 25530–25534 (2019).
  29. Zhang, N., Zhao, G., Li, L., Wang, P., Xie, L., Cheng, B., Li, H., Lin, Z., Xi, C., Ke, J., Yang, M., He, J., Sun, Z., Wang, Z., Zhang, Z. & Zeng, C. Magnetotransport signatures of Weyl physics and discrete scale invariance in the elemental semiconductor tellurium. *Proc. Natl. Acad. Sci. U.S.A.* **117**, 11337–11343 (2020).
  30. Liu, Z. K., Yang, L. X., Sun, Y., Zhang, T., Peng, H., Yang, H. F., Chen, C., Zhang, Y., Guo, Y., Prabhakaran, D., Schmidt, M., Hussain, Z., Mo, S.-K., Felser, C., Yan, B. & Chen, Y. L. Evolution of the Fermi surface of Weyl semimetals in the transition metal pnictide family. *Nat. Mater.* **15**, 27 (2016).
  31. Schoop, L. M., Topp, A., Lippmann, J., Orlandi, F., MÜchler, L., Vergniory, M. G., Sun, Y., Rost, A. W., Duppel, V., Krivenkov, M., Sheoran, S., Manuel, P., Varykhalov, A., Yan, B., Kremer, R. K., Ast, C. R. & Lotsch, B. V. Tunable Weyl and Dirac states in the nonsymmorphic compound CeSbTe. *Sci. Adv.* **4**, eaar2317 (2018).
  32. Liu, D. F., Xu, Q. N., Liu, E. K., Shen, J. L., Le, C. C., Li, Y. W., Pei, D., Liang, A. J., Dudin, P., Kim,

- T. K., Cacho, C., Xu, Y. F., Sun, Y., Yang, L. X., Liu, Z. K., Felser, C., Parkin, S. S. P. & Chen, Y. L. Topological phase transition in a magnetic Weyl semimetal. *Phys. Rev. B* **104**, 205140 (2021).
33. Belopolski, I., Cochran, T. A., Liu, X., Cheng, Z.-J., Yang, X. P., Guguchia, Z., Tsirkin, S. S., Yin, J.-X., Vir, P., Thakur, G. S., Zhang, S. S., Zhang, J., Kaznatcheev, K., Cheng, G., Chang, G., Multer, D., Shumiya, N., Litskevich, M., Vescovo, E., Kim, T. K., Cacho, C., Yao, N., Felser, C., Neupert, T. & Hasan, M. Z. Signatures of Weyl fermion annihilation in a correlated Kagome magnet. *Phys. Rev. Lett.* **127**, 256403 (2021).